IPP-Report

Max-Planck-Institut
für Plasmaphysik

Stefan Jong

Carbide Formation in Tungsten-Doped Carbon Films

IPP 17/37
Dezember, 2012

Max-Planck-Institut für Plasmaphysik
Garching bei München

&

Hochschule München für angewandte Wissenschaften
München

Carbide Formation in Tungsten-Doped Carbon Films

Stefan Jong

Abstract

Carbon (C), beryllium (B) and tungsten (W) are potential candidates as Plasma Facing Materials (PFM) for the International Thermonuclear Experimental Reactor (ITER). During operation, co-deposited layers are formed from the eroded PFM, which will grow with time. At Max-Planck Institut für Plasmaphysik, the interaction between plasma and PFM (deuterium retention and erosion behavior) are still being investigated. Hence, amorphous metal-doped carbon films (a-C:Me, Me: W, Ti, Zr, V) have been produced by dual magnetron sputtering and studied after heat treatment up to 1300K by X-Ray Diffraction (XRD), Extended X-ray Absorption Fine Structure (EXAFS) and X-Ray Photoelectron Spectroscopy (XPS). All doping metals, except for tungsten, showed clear carbide formation at 1300K using XRD.

Basic information on the phase formation on a-C:W films of the three possible tungsten carbides in the non-thermal equilibrium W-C system is required. For this study, amorphous tungsten-doped carbon films (a-C:W) were produced by magnetron sputter deposition with tungsten concentration in the range of 6 to 30 at.%. The films were then annealed at various temperatures up to 2800K. Carbide phases formed after heat treatment and their crystallite sizes were investigated by XRD. In addition, the crystallite size distribution and sample morphology were determined by a Scanning Electron Microscope (SEM) on cross-section prepared by a focused Ion Beam (FIB). Phase identification of nanometer-sized crystallites was done at TU Warsaw with nano-diffraction in a Scanning Transmission Electron Microscope (STEM) as part of co-operation.

Within the specimens, all three carbide phases, WC, W_2C and WC_{1-x}, were found by XRD as function of the two parameters, concentration and temperature. Within the lower concentrated specimens, WC_{1-x} is the dominant carbide throughout the complete temperature range. W_2C is dominant within the middle concentrated films and in the temperature range of 1450K to 2200K. WC becomes dominant for the higher concentrations and at 2500K for the middle concentrated specimens. Crystal sizes ranging from 2 nm up to 1μm were found for WC, whereas W_2C and WC_{1-x} crystals remain relative small (~15 nm). Special designed multi-layers were produced by magnetron deposition and annealed to 2200K to investigate crystal size gradient as function of the tungsten concentration. The average crystal size within the specimen increases as the tungsten concentration increases within the specimen.

The results from this investigation can be used to design specimen/coatings with desired specifications, i.e. carbide phase and crystallite size. Industrial applications with the results from this investigation remain unknown.

Zusammenfassung

Für die Beschichtung (PFM) der ersten Wand des International Thermonuclear Experimental Reactor (ITER) sollen die Elemente Kohlenstoff (C), Beryllium (B) und Wolfram (W) verwendet werden. Während des Betriebes des Reaktors wird das Wandmaterial langsam erodiert und lagert sich an anderer Stelle als Mischmaterial wieder ab. Dies hat Einflüsse auf die Eigenschaften des Wandmaterials im Reaktor. Aufgrund dessen wird am Max-Planck Institut für Plasmaphysik seit einigen Jahren die Wechselwirkungen zwischen dem Plasma und der Reaktorwand untersucht. Dabei wird ein besonderes Augenmerkt auf das Rückhalte- bzw. Erosionsverhalten von Deuterium bzw. von Mischmaterialen gelegt. Um die Wechselwirkungen zu analysieren, wurden metalldotierte Kohlenstoffschichten (a-C:Me, Me: W, Ti, Zr, V) durch reaktives Magnetronzerstäuben hergestellt und anschließend bis auf 1300K aufgeheizt. Die Kristallstruktur der geheizten Proben wurde daraufhin mit XRD, NEXAFS und XPS untersucht. Allen verwendeten Metalle, ausschließlich Wolfram, bildeten Kristalle, die im XRD bei 1300 K deutlich erkennbar waren.

Um dieses Verhalten zu erklären, werden allgemeingültige Grundlagen für die Phasenbildung der Wolframkarbid in a-C:W Schichten für ein nicht-thermodynamisches Gleichgewicht benötigt. Für diese Arbeit wurden amorphe, wolframdotierte Kohlenstoffschichten durch Magnetronzerstäuben mit einer Wolframkonzentration zwischen 6 und 30 at.% hergestellt und bis auf Temperaturen von 2800 K geheizt. Im Anschluss an den Heizprozess wurden die Proben mittels XRD auf ihre Kristallstruktur und -größe untersucht. Zusätzlich wurden die Kristallgrößenverteilung und die Oberflächenmorphologie im SEM analysiert. Dazu wurden Profilschnitte mit dem FIB erstellt. In Kooperation mit der Technischen Universität von Warschau wurden die Phasen der nanometergroßen Kristalle charakterisiert.

Alle drei Karbidphasen, WC, W_2C und WC_{1-x} wurden in Abhängigkeit der Anlasstemperatur und Wolframkonzentration durch Röntgenbeugung detektiert. In den Proben, die eine niedrige Wolframkonzentration aufweisen, dominiert die WC_{1-x} Phase. Die W_2C Phase liegt hauptsächlich in den Proben mit mittlerem Wolframgehalt (10 bis 18 at.%) bei einer Temperatur zwischen 1450 und 2200 K vor. Ab einer

Ausheiztemperatur von 2500 K dominiert die WC Phase. In den Proben mit hoher Wolframkonzentration bildet sich ausschließlich des WC Phase aus. Die Kristallgröße variiert in den unterschiedlichen Karbidphasen zwischen 2 nm und 1 µm. Mit der Untersuchung speziell gebildeter Multischichten wurde der Zusammenhang zwischen der Kristallgröße und der Wolframkonzentration bestätigt. Mit steigendem Wolframanteil nimmt die durchschnittliche Kristallgröße zu.

Die Ergebnisse dieser Studie können für die Erstellung von Proben bzw. Beschichtungen mit definierten Eigenschaften (Karbidphasen, Kristallgröße) genutzt werden. Aussagen über den industriellen Nutzen können jedoch nicht getroffen werden.

Content

Abbreviations

a-C:W	Amorphous tungsten doped carbon films.
BSE:	Backscattered Electrons
CFC:	Carbon Fibre Reinforced Carbon
DC:	Differentiating Current
EDX:	Energy Dispersive X-Ray
EXAFS:	Extended X-ray Absorption Fine Structure
FIB:	Focused Ion Beam
FWHM:	Full Width Half Maximum
GID:	Grazing Incidence Diffraction
IBA:	Ionic Beam Analysis
ICDD:	International Centre for Diffraction Data
IPP:	Institut für Plasmaphysik
ITER:	International Thermonuclear Energy Reactor
JET:	Joint European Torus
LMIS:	Liquid Metal Ion Source
NEXAFS:	Near-Edge X-ray Absorption Fine Structure
PDF:	Windows Powder Diffraction File
PFM:	Plasma Facing Material
PVD:	Physical Vapour Deposition
RBS:	Rutherford Backscattering
RF:	Radio Frequency
SE:	Secondary Electrons
SEM:	Scanning Electron Microscope
SIMNRA:	Simulated Nuclear Reaction Analysis
STEM:	Scanning Transmission Electron Microscope
WC:	Tungsten Carbide
W_2C:	Tungsten Carbide
WC_{1-x}:	Tungsten Carbide
PDF:	Windows Powder Diffraction File
XPS:	X-Ray Photoelectron Spectroscopy
XRD:	X-Ray Diffraction

Chapter 1

1. Introduction

Supplying a growing world population with energy is one of the challenges mankind has to face in the next couple of decades. The International Energy Agency (IEA) estimates that the world's primary energy demand will increase by 60% from 2002 to 2030. 80% of the total energy used then will come from fossil fuels (mainly oil and coal), while the remaining energy will come from nuclear power and renewable energy sources (e.g. wind, solar, geothermal, hydro) [1]. Although estimates show that enough resources are still found within Earth's crust for another few decades, alternative energy sources have to be found.

Besides depleting oil, coal and natural gas reserves, effects of global warming and natural disasters (e.g. Deep See Horizon and nuclear reactor Japan) will force us to change our energy production/consumption to reduce the emission of greenhouse gasses.

Candidates to supply the world with energy are: geothermal, solar, nuclear fission and nuclear fusion. Due to disposal problem, military usage and safety issues (e.g. Japan) nuclear fission is not seen as a long term energy supply. If geothermal and solar are able to supply the world's energy demand in the future is debatable, an alternative is seen in nuclear fusion.

1.1 Nuclear Fusion

Nuclear fusion, the process that takes place in our suns core, is the process of melding lighter atoms in a heavier atom under great gravitational forces. Fusion uses the principle of mass deficit, where the protons and neutrons that are fused together each give up a little mass. The mass of the new formed nucleon is lighter as the initial sum of atoms that undergo fusion; the small loss of mass is converted in tremendous amount of energy.

Scientists from around the world are trying to make fusion reactions possible here on earth, creating a safe and sustainable energy source. For laboratory fusion power, the following nuclear reactions are of interest.

Table 1.1: List of possible fusion reactions with hydrogen isotopes and their products with kinetic energy.

$$D^+ + D^+ \longrightarrow {}^3He^{++}\left(0.82MeV\right) + n^0\left(2.5MeV\right) \tag{1.1}$$

$$D^+ + D^+ \longrightarrow T^+\left(1MeV\right) + p^+\left(3MeV\right) \tag{1.2}$$

$$D^+ + {}^3He^{++} \longrightarrow {}^4He^{++}\left(3.6MeV\right) + p^+\left(14.7MeV\right) \tag{1.3}$$

$$D^+ + T^+ \longrightarrow {}^4He^{++}\left(3.5MeV\right) + n^0\left(14.1MeV\right) \tag{1.4}$$

From the 4 reactions above, scientists have found that the most efficient fusion reaction to produce the ‘most’ energy at the ‘lowest’ temperatures on earth is equation 1.4 [2].

The fuel that powers this fusion reaction consists of the hydrogen isotopes; Deuterium (D) and Tritium (T). Deuterium, a harmless isotope found in water, can be found globally around the world. In every liter of water, 33 milligram of deuterium can be won through distillation; hence deuterium is seen as a virtual inexhaustible resource. Tritium, however, a radioactive isotope of hydrogen, cannot be won from water due to the scarceness (nearly zero). This would make extracting tritium from water difficult and very expensive. Other methods, to win tritium as fuel are being looked at. The most distinct way to win tritium is by breeding tritium by neutron capture through so called lithium blankets, which is been considered for the ITER reactor [2].

Even though the reaction (1.4) requires the ‘lowest’ fusion temperature, temperatures of 150,000,000°C are still needed for this reaction to take place. The heat generated by the collision of the plasma particles within the vessel and ohmic heating do not suffice to reach high enough core temperatures. Two optional external heating methods are available, which will complement standard methods to reach high enough core temperatures. These methods are neutral beam injection and high-frequency electromagnetic waves [2]. With the external heating methods, high enough temperatures can be achieved, making fusion between the isotopes possible.

The Iternational Thermonuclear Energy Reactor (ITER) is a large scientific experiment to illustrate the world that it is possible to produce commercial energy from nuclear fusion. Other fusion devices, Joint European Torus (JET) and ASDEX-Upgrade, both partners of ITER, have tested plasma properties and proven that fusion on earth is possible. JET was the first reactor to achieve fusion power in 1997; however the device required more energy than the reaction produced. ITER will be the first reactor where a net energy will be created, proving that it is possible to capture fusion energy for commercial usage. Capturing energy, ITER will test key technologies, as described above, for future reactors. Figure 1.1a is a cross-section of the ITER tokomak fusion reactor which is under construction in South France, Cadarache. Figure 1.1b shows a close-up of the plasma vessel with the Plasma Facing Material.

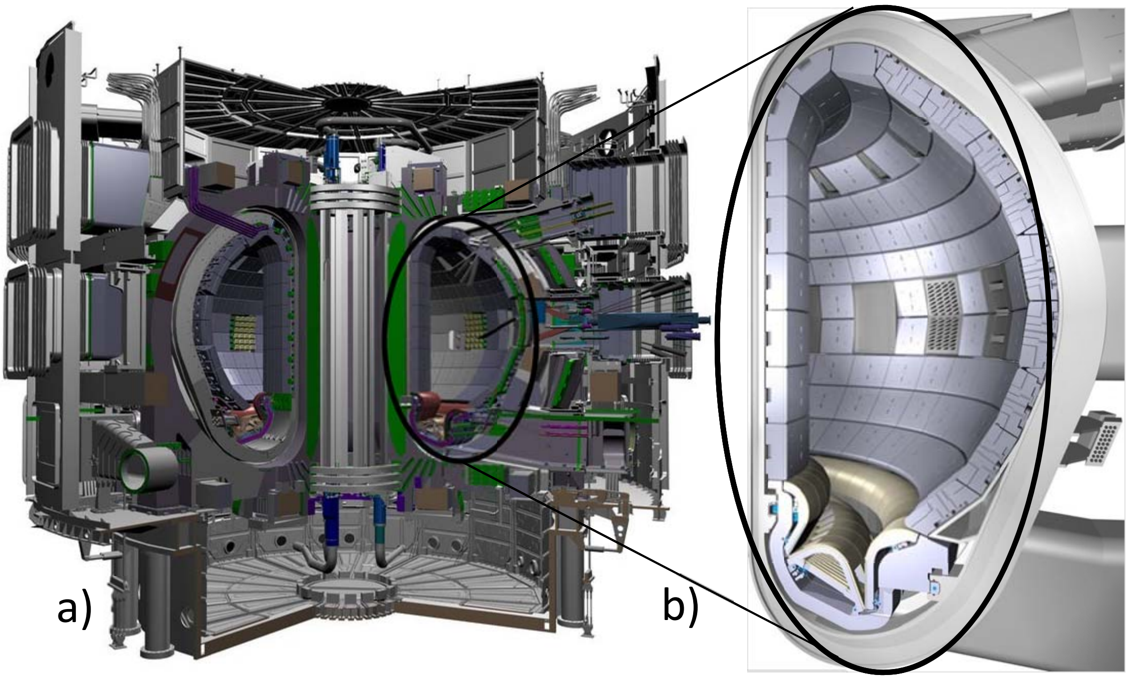

Figure 1.1: a) A cross-section of the complete ITER fusion device being designed to generate future fusion power. b) A close-up of the tokamak vessel with Plasma Facing Material (PFM). [a]

During operation, the reactor wall eventually becomes radioactive, due to activation of the wall materials by neutron irradiation. In addition, there will be a small amount of tritium retention in the wall material. The amount of radioactive waste generated from a fusion reactor is relative small compared to a fission reactor. Additionally, the decay time and radiation levels of the formed isotopes in the reactor are considerable lower than those of a fission reactor. Hence, the products won't have to be stored into deep underground bunkers for preservation and safety of the environment.

Besides radioactive safety concerns, the hot plasma is also a thread to the machine, since no material can withstand direct contact with such extreme high temperatures. Although lower temperatures are measured at the vessel boundary, high heat fluxes are still there eroding the PFM (Plasma-facing Material). To increase the lifetime of the wall components during operation, a suitable PFM is needed.

1.2 Plasma Facing Material

During operation, the PFM (Plasma Facing Material) has to withstand immense temperatures and pressures and degradation from particle impact. Carbon materials have been applied in many fusion reactors for optimal performance. Carbon materials, graphite and Carbon fibre reinforced Carbon (CFC) show strong mechanical properties, good thermodynamic properties and do not melt. Therefore, carbon materials were seen as the ideological choice as PFM. Unfortunately, carbon materials have three drawbacks.

1. CFC shows strong chemical reactivity with hydrogen, leading to high erosion yields under hydrogen impact. This drastically reduces the lifetime of the wall components, which have to be replaced frequently [3, 4, 5].
2. The possible threat of hydrogen retention, especially in the case with radioactive tritium will lead to safety concerns in the co-deposited layers. [3, 5]
3. Over time neutron damage will change the physical properties of graphite making it brittle and break up. During operations this could lead to disasters.

Another concern with carbon is plasma impurity. Since carbon is a low Z element, it is easily sputtered and ionized within the plasma. The ionization of carbon by the plasma reduces the core plasma temperature.

To reduce plasma impurities, radiation loss of the plasma, and hydrogen retention, a mixture of carbon and metals have been considered [4]. Low Z elements, in the case of ITER; beryllium ($Z=4$) and carbon ($Z=6$), are foreseen for PFM, since they lead to lower cooling of the core plasma via radiation. Besides lower plasma cooling after being eroded, beryllium has the advantage of being a good oxygen getter. Low Z elements are easier eroded than high Z elements, reducing the lifetime of the wall components. To increase the lifetime of the wall components, high Z elements are used. In addition they are more durable against heat loads and particle bombardment [5]. The disadvantage of high Z elements is that they are more harmful for the core plasma via radiation, leading to cooling of the plasma.

1.3 Aim of Work

Over the last years, chemical erosion by hydrogen impact of doped graphite as well as the re-erosion of deposited mixed films in fusion plasma devices have been studied in detail at IPP and other institutes. The investigation and result have led to the publications of several papers, thesis and dissertations (summarized in [6]).

One of these publications that studied the erosion behavior of mixed layers and particularly the characterization of a-C:Me structures in detail was by Christoph Adelhelm [3]. In his work three different parameters were investigated: Metal type (Ti, V, Zr, W), metal concentration (<15%) and annealing temperatures up to 1300K. The choice of metals was mainly based on the material choice of ITER (W) and possible dopant elements on graphite (Zr, V, Ti). Low concentrations were used, as they already suppress the erosion behavior severely.

Annealing these samples lead to the formation of TiC, ZrC and VC crystallites in case of Ti, Zr and V- doping, what was shown by multiple characterization techniques: XRD, XPS, EXAFS and NEXAFS. These findings correspond to the information from the phase diagram of Ti-C, Zr-C and V-C. However, characterizations up to 9.5% a-C:W film with XRD lead to no identification of possible crystallographic carbide, as only broad peaks could be observed in the diffractogram. NEXAFS spectra revealed W_2C after annealing to 1300K and XRD diffraction showed WC only after annealing to 1700K. The findings from these techniques contradict to the expected answers for the W-C phase diagram, see section 2.5. While Ti, Zr and V had built clear crystal structures up to temperatures of 1300K, tungsten still had very small crystallites. In addition all three metals formed their stable thermodynamic equilibrium carbide phase, whereas tungsten was only found in a meta-stable thermodynamic carbide phase at 1300K.

In this presented work, the investigation of carbide formation in doped a-C:W films will be done. a-C:W films were produced by magnetron sputtering, with a tungsten concentration between 6 at% and 30 at%. The samples were annealed inside a high temperature graphite oven at temperatures from 1300K up to 2800K. After heat treatment, the samples were investigated mainly using XRD. Other techniques as SEM, STEM and nano diffraction were also applied.

This research will give a better understanding about the carbide formation of a-C:W films, and support the findings by Christoph Adelhelm [3].

Chapter 2

In the following chapter, the methods used to produce and characterize the samples will be discussed: Magnetron sputtering, Rutherford-back scattering, SEM and nano-diffraction and XRD. Since the XRD is the main examining method throughout this work, a more detailed description will be given than for the other methods. Besides these methods the W-C phase diagram will be illustrated to understand the formation of tungsten carbide in a thermodynamic equilibrium.

2.1 Magnetron Sputter Deposition

Magnetron Sputtering is a physical vapour deposition (PVD) method used to create thin films. Film production by PVD is important in modern industrial sectors, as it is applied to obtain hard, wear resistance coatings. PVD is done in a vacuum environment since it is based on the creation of a vapour by physical means and condensation on a desired material. During sputtering the vapour is created by ion impact on a cathode. Magnetron sputtering is widely used by industries as nearly all elements can be deposited, every composition/concentration can be achieved and the thickness of the coating to be controlled.

Magnetron sputtering of materials is based on charged ions which bombard a target, acting as a cathode for the plasma discharge. Argon is by far the most widely used projectile for sputter deposition of thin films. Once an ion collides with the target, energy is transferred to the atomic nuclei. If the impact energy transferred to the surface atom is larger than the surface binding energy, an atom is ejected (sputtered) [7]. The ejected atom now deposits on specimen holder, where the samples are arranged, where it creates a thin film. More details on the underlying process leading to a sputtered atom surface can be found in [8].

Depending on the material which has to be sputtered, a DC or RF voltage is applied to the cathode. In case of semiconductors, a DC power supply can be used. For isolators a RF or pulsed DC power supply must be used. Both DC and RF sputtering, where the plasma is simply created by a DC or RF discharge, suffer from low deposition rates, due to low argon ionization within the plasma.

The most important quantity for describing the deposition rates during sputtering process is the sputtering yield Y. The sputtering yield is defined as the average number of atoms removed from the surface of a solid per incident particle. The sputtering yield depends on the mass, the energy, and the impact angle of the incident particles; on the mass and the binding energy of the atoms in the solid as well as at the surface; and on the crystallinity and crystal orientation of the solid.

One way to increase the sputtering rate for the target, i.e. the deposition rate at the sample, is by applying a magnetic field around the cathode, figure 2.1. The magnetic field traps electrons close to the target resulting from a DC or RF discharge. The electrons follow a helical path around the magnetic field lines, increasing the plasma density above the target. Denser plasma enhances the ionization of the argon gas, leading to higher sputter rates. Besides increasing deposition rates, the plasma can also be sustained at lower pressures.

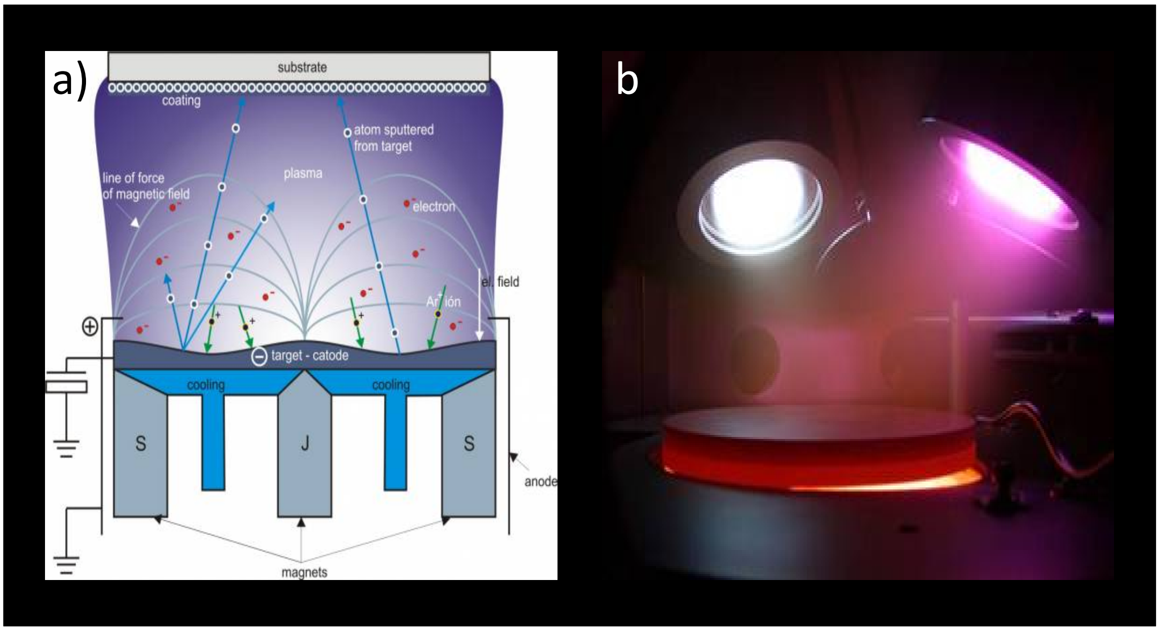

Figure 2.1: a) detailed illustration of the setup of a magnetron sputter device with magnetic field lines [20]. b) A photo of the inside of a dual magnetron device during deposition. The white and purple light comes from the plasma [21].

Due to the high deposition rates reached by magnetron sputtering, some of the inert sputtering gas can remain trapped within the deposited layer. This is verified by a spectrum made with RBS (Rutherford Backscattering Spectroscopy), as shown in Figure 2.2. Beside some Argon getting trapped within the layer, high deposition rates may result in high tension within the layer. This can result in the delaminating / pealing-off of the deposited layer.

2.2 Rutherford Backscattering Spectroscopy (RBS)

Rutherford Backscattering Spectroscopy is an Ion Beam Analysis (IBA) technique that provides information about the distribution of mass as a function of depth. RBS is the most precise and simple method to obtain information about absolute concentrations and composition of the film up to some ten of microns. Depth information is provided by the energy loss of the projectiles on their inward and outward paths through the sample. The technique is also extremely useful in profiling layered structures. For this purpose, a monochromatic MeV ion beam of light atoms (mostly ^{4}He 0.4-4 MeV) is created by an accelerator and projected onto the samples surface. The number and energy distribution of backscattered particles is measured with a detector located at a distinct given angle. [9] The ratio of energy the before (E1) and after (E2) incident only depends on the mass of the projectile and the target mass (M1, M2) as well as on the scattering angle θ. The ratio, also known as the kinematical factor, is given in equation (2.1) and allows the target element to be identified [9].

$$\frac{E_2}{E_1} = K = \left(\frac{M_1 \cos\theta}{M_1 + M_2} + \left[\left(\frac{M_1 \cos\theta}{M_1 + M_2} \right)^2 + \frac{M_2 - M_1}{M_1 + M_2} \right]^{1/2} \right)^2 \tag{2.1}$$

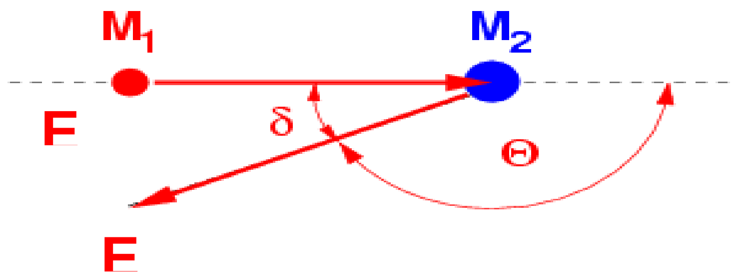

Figure 2.2: Rutherford Back-Scattering, where projectile M_1 with energy E_1 hits target atom M_2 scattering M_1 at an angle θ with energy E_2 [22].

This equation is only valid if the angle between incident/scattered directions δ is very small and at the outermost surface of the sample. At greater depths stopping power leads to depth information. Stopping power causes the projectiles to loss energy in form of excitation or ionization of target electrons, therefore changing the kinematic ratio and target atom. Without any knowledge about the composition of the sample, it is hard to determine the target atom. Stopping power is a statistic process resulting in straggling.

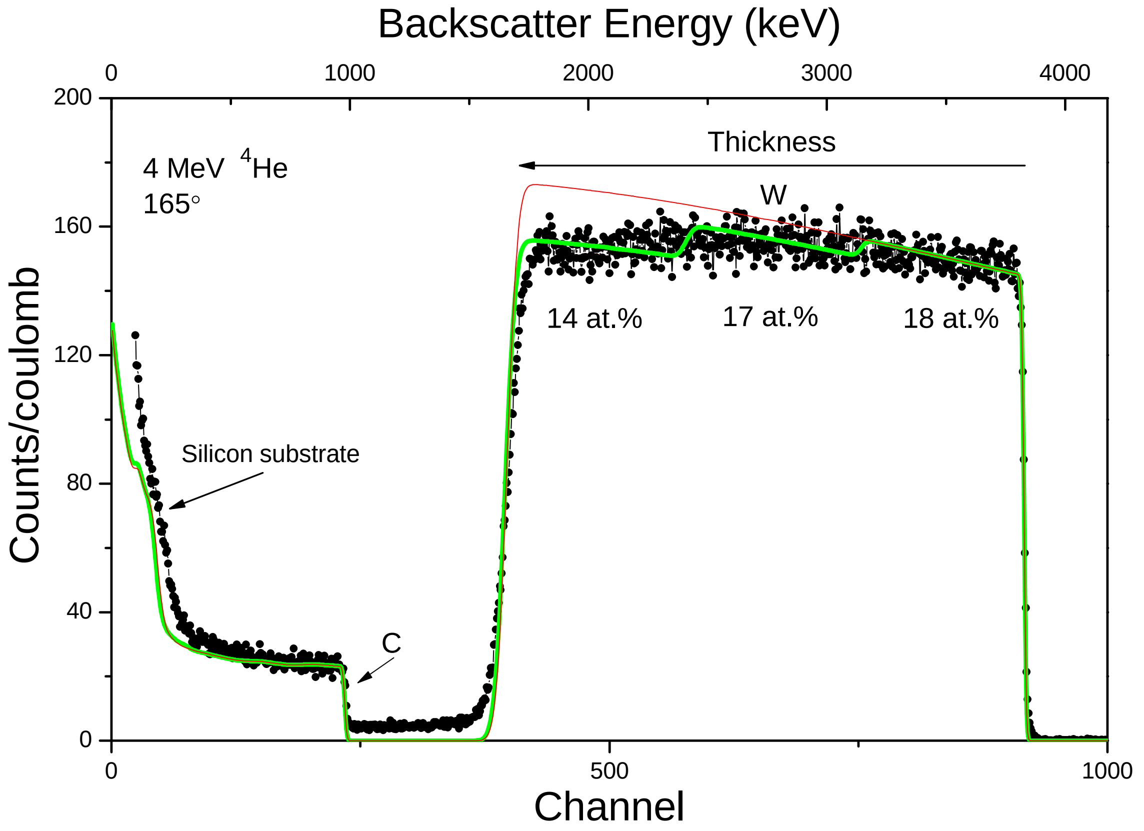

Figure 2.3: An RBS spectrum of a 18% a-C:W film on a silicon substrate. The general thickness (atoms/cm^2) as well as the concentration can be determined by fitting a simulated spectrum.

Figure 2.3 shows a spectrum of a 18% a-C:W film on a silicon substrate. The atomic mass difference of the target atoms lead to different peak positions within the spectrum. The different target atoms and their concentration as well as the general layer thickness of the film can be obtained by fitting a simulated spectrum to the measured data. SIMNRA (SIMulated Nuclear Reaction Analysis) is such a program capable of simulating spectra to the measured data and is used in this thesis [10]. In figure 2.3 two different simulated spectrums have been fitted to the measured data. A homogenous 18 at% W concentrated film is expressed by the red line, whereas the green line expresses a rough simulated fit to the measured data. As observed for the samples, the concentration in the lower layer is smaller than the surface concentration, due to start-up process of the sputter device. The specimens of the different production runs are named by their concentration levels at the surface, e.g. 18% a-C:W stands for 18 at% tungsten-doped amorphous carbon film. The lowering of the concentration as function of depth has to be kept in mind [7].

2.3 Microscopy

2.3.1 Scanning Electron Microscopy (SEM)

A scanning electron microscope is a microscope that uses electrons rather than light to image surfaces. Since electrons are used, SEM has to operate in a vacuum environment and the specimen must have a certain electrical conductivity. The electrons produced by an electron gun are focused using electromagnetic lenses. Deflector plates are used to scan the very narrow electron beam in x and y direction to allow scans in raster pattern. The electrons interact with the atoms of the sample, producing signals containing information about the sample's surface. The signals produced after interactions include: secondary-electrons (SE), Backscattered electrons (BSE) and Energy Dispersive X-ray (EDX). The signal are captured by detectors and processed into an image.

There are many advantages to using a SEM compared to a standard light microscope:

(i) A SEM has a large depth of focus as result of the very narrow electron beam, generating a characteristic three-dimensional image.

(ii) SEM can produce high resolution images, allowing closely spaced features to be examined at high magnification. Nowadays commercial SEM reach resolutions in the nanometer range.

(iii) Magnification levels can be varied by 6 orders of magnitude reaching viewing areas between 1 mm^2 and 1 μm^2 Magnifications from 10.000 to 500.000 times can be used in a SEM. This is useful for understanding the surface morphology and topography of a sample.

(iv) SEM can deliver any information about the chemical composition of the sample.

2.3.2 Focused Ion Beam (FIB)

The Focused Ion Beam is a technique used for site-specific analysis, deposition and ablation of materials. ‘The FIB instrument consists of a vacuum system and chamber, a liquid metal ion source, an ion column, a sample stage, detectors, gas delivery system and a computer to run the instrument’ [11]. The FIB shows many similarities in forming the beam compared to a SEM. However a FIB uses an ion column instead of an electron column.

‘The capabilities of the FIB for small probe sputtering are made possible by the liquid metal ion source (LMIS)’ [11]. The LMIS is a tungsten needle or spiral, where the liquid metal is contained. Tungsten is chosen due to its high melting point. From all metallic elements and alloy sources available, gallium (Ga) is the most commonly used LMIS in FIB instruments, as gallium has the lowest melting point of all metals and alloys. The molten Ga flows towards the tip of the tungsten needle. An electrical field, applied to the end of the tip causes gallium ion emission which are then accelerated through the ion column.

Commercial FIB now possess both electron and ion column, hence a FIB may sometimes have been incorporated into an SEM (FIB/SEM), known as a dual-beam system. In the typical dual-beam column the electron column is mounted vertical and the ion column is tilted. The ion column is in most configurations tilted under an angle of around 50° For FEI instruments the angle between electron and ion column is 52° to the vertical. For milling normal to the samples surface, the sample is tilted 52°. Figure 2.4a illustrates a typical dual-beam configuration. This configuration is used for cross-sectioning in this work.

By altering the ion flux, a FIB can be used for two purposes. A FIB can be used for sampling the surface of specimen for low energy ions or for precise sputtering of a selected area of the sample with high energy ions. The controlled sputtering of the sample by gallium ions allows cross-sections to be made. Figure 2.4b is an actual cross-section made by a FIB/SEM for sample analysis of an 9% a-C:W film annealed to 2800K as illustrated within figure 2.4a. The surface has been coated with a platinum-carbon coating, which has been added to protect the sample surface during sputtering and reduce artifacts on the cross-section surface due to the ion beam profile. During the sputter process, a trench is created making it possible to see the cross-section with the SEM column. Underneath the Platinum-carbon coating is the FIB cross-section. A more detailed description of this cross-section can be found on the next page.

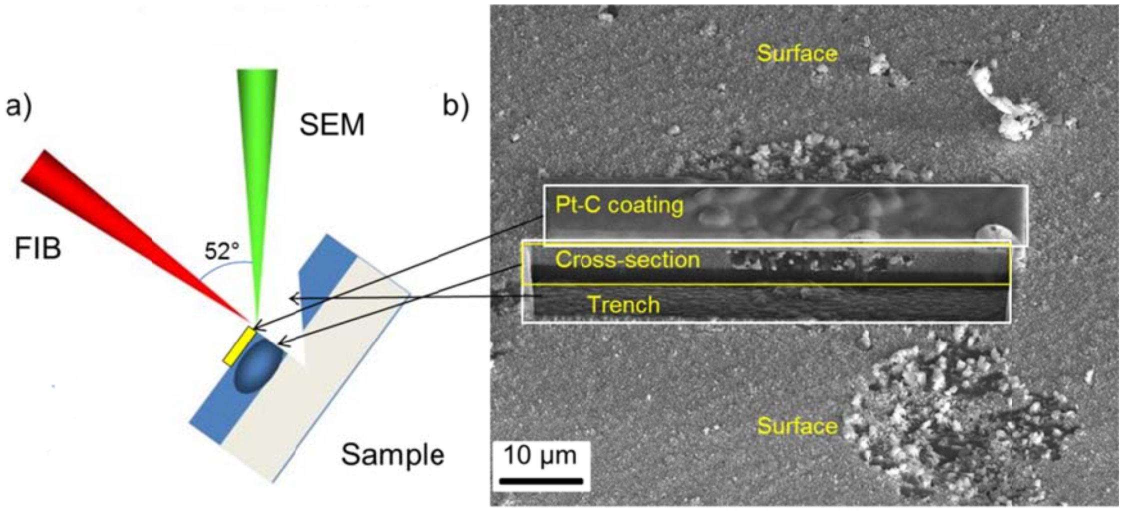

Figure 2.4: a) Dual-beam configuration of a FIB/SEM instrument. b) Cross-section made by a FIB/SEM instrument of a a-C:W deposition as seen in illustration.

Figure 2.5, shows a close up of a cross-section similar to the cross-section in figure 2.4b. At the bottom of the cross-section, a homogenous black area can be found representing the UC graphite substrate used during the deposition run. Above the substrate, the a-C:W film can be found. Within the a-C:W deposition, small white dots, tungsten-carbides formed after heat treatment, can be found randomly distributed throughout image. The black area around the carbides is amorphous carbon. On top of the a-C:W deposition a light grey area can be seen, representing the platinum-carbon coating.

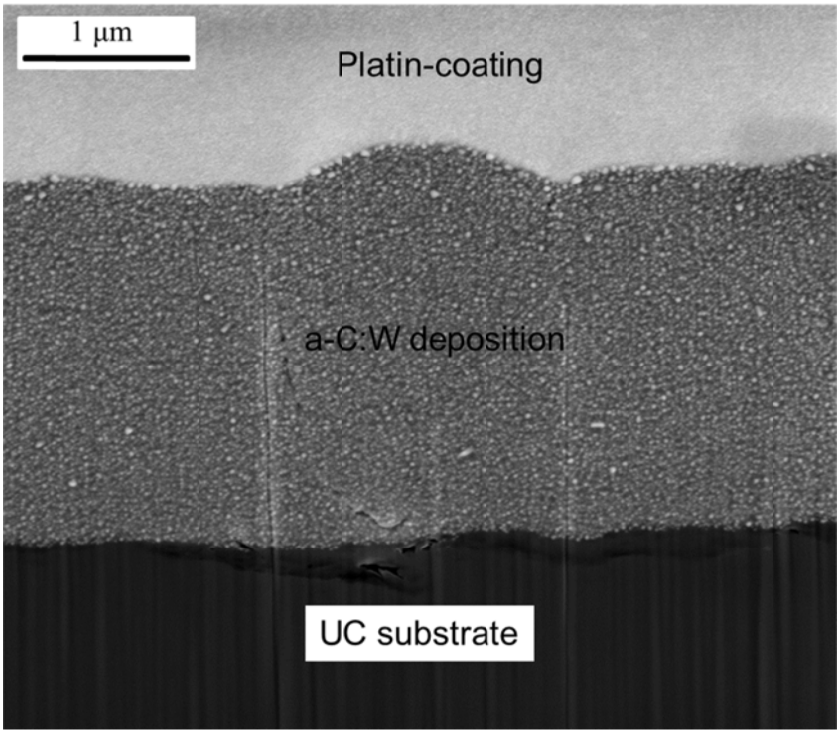

Figure 2.5: a detailed cross-section made by a FIB/SEM, showing the main areas of information.

2.4 X-ray Diffraction (XRD)

2.4.1 Setup

X-ray diffraction is an analysing method with a wide field of applicability. In its early years the technique was only used for the determination of crystal structures. The method is nowadays used for the determination of chemical phase analysis, stress measurements, the study of phase equilibria, measurement of particle size and textures [12]

X-ray diffraction uses the principle of elastic scattering (Thomson scattering) of x-ray radiation by electrons. In this process the 'electron oscillate like a Hertz dipole at the frequency of the incoming x-ray beam and become a source of dipole radiation' [12]. During this process the wavelength λ of the x-rays is conserved. Diffraction effects, explained by destructive and constructive interference, are observed on periodic structures, where the interatomic distances in crystals and molecules correspond to the wavelength of the x-rays. [13].

The Bragg equation (2.2) describes the relation between the lattice plane distance d and the incident angle θ of x-ray wavelength λ (e.g. 0.154 nm for Cu $K\alpha$).

$$2d \sin \theta = n\lambda \tag{2.2}$$

Figure 2.6a illustrates that constructive interference only occurs when the phase shift of $2d \sin \theta$ between two incoming x-rays is an n fold of the incident wavelength.

A frequently used technique for measuring Bragg reflection is the $\theta/2\theta$ configuration. Here the XRD diffraction pattern is obtained by changing the x-ray incident angle by θ, while the scattering angle is moved by 2θ.

The main difficulty with diffractometers is dealing with a divergent beam emitted by an x-ray tube. Controlling the x-ray beam bundles in $\theta/2\theta$ diffractometers is performed by slits and apertures as traditional lenses and other refractive elements used for visible light do not work on x-ray radiation. The most frequently setup using slits and aperture is the so-called Bragg-Brentano or parafocusing mode. Figure 2.6.b illustrates a schematic setup of a $\theta/2\theta$ diffraction in Bragg-Brentano geometry. Important with Bragg-Brentano geometry is that source and detector both are located on the goniometer circle. The x-ray bundles are only focused in the Bragg-Brentano geometry when the goniometer circle intersects the focusing circle. For constant focusing the sample need to be bended so that for every angle, the focusing circle intersect the goniometer circle. [13] Unfortunately the radius of the focusing circle varies with different scattering angle.

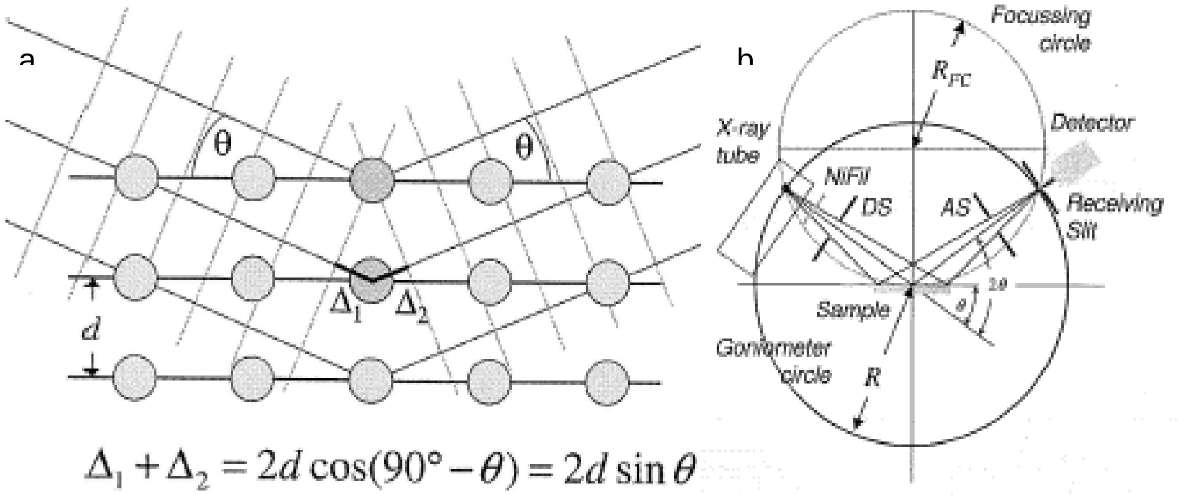

Figure 2.6: a) derivation of the Bragg-equation, showing the relation between the lattice distance *d* and incident angle *θ* [13]. b) The Bragg-Brentano measurement setup used for x-ray diffraction. True focusing is only possible at the intersection of the focusing circle and goniometer circle. All other positions are in parafocusing mode [13].

Another commonly setup used for determining crystal structure is Grazing Incidence Diffraction (GID), applied on thinner films [13]. Due to high penetration depths of x-ray radiation (few microns), the majority of the diffraction comes from the substrate and not from the phases present in thin films. The combination of low diffracted signal and high background make it very difficult to identify carbide phases present. To increase the path length of the incident X-ray beam through the film small incident angles are used, so that conventional structure identification can be done. The increased path length increases the intensity from the film and lowering that of the substrate. Besides small incident angles, the x-ray radiation will need to be nearly parallel for GID. To achieve parallel radiation, a multilayer is used with a parabolic mirror (Göbel Mirror) inside. The multilayer also has the advantage of filtering the Cu *Kβ* radiation. Horizontal and vertical slits are used on the multilayer to collimate the x-ray beam. The nearly parallel beam is diffracted and enters a GID attachment with several slits, a vertical plate arrangement which allows complete parallel x-rays to pass while absorbing converging and diverging diffracted x-rays. This slightly reduces the intensity measured on the detector side. A disadvantage using thin plate arrangement is the wide instrumental peak. Nonetheless, it is the fastest method due to high intensities for obtaining crystal structure data.

2.4.2 Crystal size

XRD is primarily used to determine the carbide phases within a film, but it also allows determination of the crystal size. The average crystallite size *D* within the film can be calculated by applying the Scherrer equation (2.3) [13]. The Scherrer equation correlates the width of the peak and the dimension of the crystallites, with $\beta_{2\theta}$ being the FWHM of the diffracted peak, θ_0 the diffraction angle and λ the incident wavelength.

$$D = \frac{0.93\lambda}{\beta_{2\theta} \cos \theta_0} \tag{2.3}$$

The Scherrer equation assumes that peak-broadening is caused by mono-dispersed cube shaped very small crystallites. However other factors, such as strains, shape distribution and crystal shape, also contribute to peak-broadening, making the calculated values for the crystal sizes too small. For example, the values for mono-dispersed spherical crystallites are 1/1.0747 too small when calculated with the Scherrer equation.

The Scherrer equation is limited in calculating the crystal size by the width of the peak. The crystal sizes can range from very small crystallites (~5nm) up to large crystals (~200nm). The crystal sizes were calculated using GID and Bragg-Brentano configuration. For the larger crystals Bragg-Brentano is used due to higher intensity, however due to instrumental peak-broadening it is impossible to distinguish the actual width above a certain sizes.

The crystal sizes calculated with the Scherrer equation should be considered to be a rough estimate, since many factors influence peak broadening and, therefore, the crystal size. Nonetheless, the growth process of crystal sizes after annealing can easily be observed with the Scherrer equation and change in peak widths.

2.4.3 Textures

Each grain normally has a crystallographic orientation different from that of it neighbor grain. Within an ideal sample, the orientation of all the grains may be randomly distributed in relation to a reference grain. Nevertheless, in the most real specimen the grain order in a preferred orientation, e.g. by the growing process, mechanical treatment or by aligning in groups inside a powder, known as texture. From the XRD diffractogram, the presence of textures can be assumed by comparing the height of the diffraction peaks with those from a database (e.g. ICDD WINPDF), see section 2.4.4. Big differences tend to be a sign of textures.

The standard XRD diffraction patterns are measured with a $\theta/2\theta$ setup, where the lattice planes are orientated parallel to the film surface. In order to determine orientation distribution (texture), all grains within the sample must be measured. This is done by rotating the sample around the azimuth angle $\left(0^\circ \le \phi \le 360^\circ\right)$ and the tilt angle $\left(0^\circ \le \psi \le 90^\circ\right)$ for a fixed incident angle θ and reflection angle 2θ. The results from texture measurements are displayed within a pole figure [13]. In this work only a comparison to the PDF file results were done in order to obtain an indication for texture of the carbide grains.

2.4.4 ICDD database

WINPDF (Windows Powder Diffraction File) is an International Centre for Diffraction Data (ICDD) database file used for peak identification for individual crystal phases [14]. As constructive interference depends on the distance between the lattice planes, i.e. the crystal structures, and reflection power of the atoms, i.e. the arrangement of the atoms in the unit cell, the reflected diffraction peaks are unique for each material. Within the WINPDF file, data about the reflected diffraction peaks along with corresponding miller indices of any material combination measured, as well as theoretical diffraction peaks of texture free, i.e. ideal powder, have been stored. In addition to the diffraction angles, the relative diffracted intensity for each peak is given. Any irregular intensity distribution in the pattern might be a sign for texture. The used PDF's in this thesis are: 4-806, 25-1047 for WC, 35-776 for W_2C, 20-1316 for WC_{1-x} and 20-1324 for WO_3.

2.4.5 Phase characterization

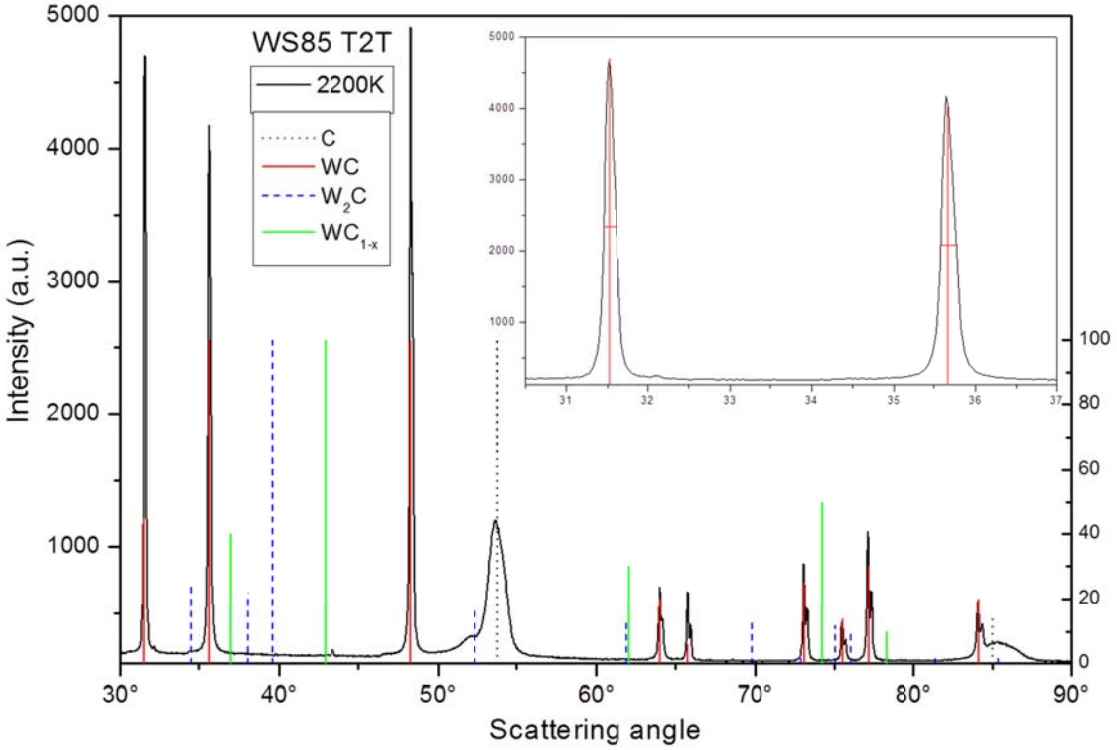

Figure 2.7: XRD diffractogram from a 2200K 22% a-C:W film investigated using a *θ/2θ* scan.

Figure 2.7 illustrates a XRD diffractogram, where the scattered intensity is plotted as function of 2θ (scattering angle). On the right axis, the relative intensity of the peaks is shown in relative percentage from. By comparing peak positions with those from the PDF-file, phases can be allocated. Within figure 2.7, peaks can be found around the red lines (WC) and the black (C), whereas no diffraction is observed around peaks from W_2C (blue) and WC_{1-x} (green). This means only WC is present within the sample, as the carbon reflection comes from the graphite substrate.

In the upper right corner the FWHM of WC peaks around 31° and 35° are show used for calculating the relative crystal size with the Scherrer equation within the sample. Before the FWHM can be calculated, the diffractogram had to be modified using a program (e.g. Analyze), allowing background subtraction, Rachinger correction and smoothing. The Rachinger correction suppresses the $K_{\alpha 2}$ x-rays from the spectrum.

2.5 W-C phase Diagram

Within the W-C phase-diagram (figure 2.8), three different kinds of carbides (Figure 2.9) can be formed in an eutectic system depending on the C-composition. These three carbides are:

- The hexagonal stoichiometric monocarbide WC.
- The cubic carbide WC_{1-x}.
- The hexagonal close packed W_2C.

From these phases, WC is thermodynamically the more favorable carbide around room temperatures. The reason is that the bonding enthalpy ΔG_f of WC is lower than that of WC_{1-x} and W_2C [15]. The other carbides, WC_{1-x} and W_2C, are thermodynamically stable around respectively 1300K to 2800K at tungsten concentrations of approximately 50 at% and 70 at%.

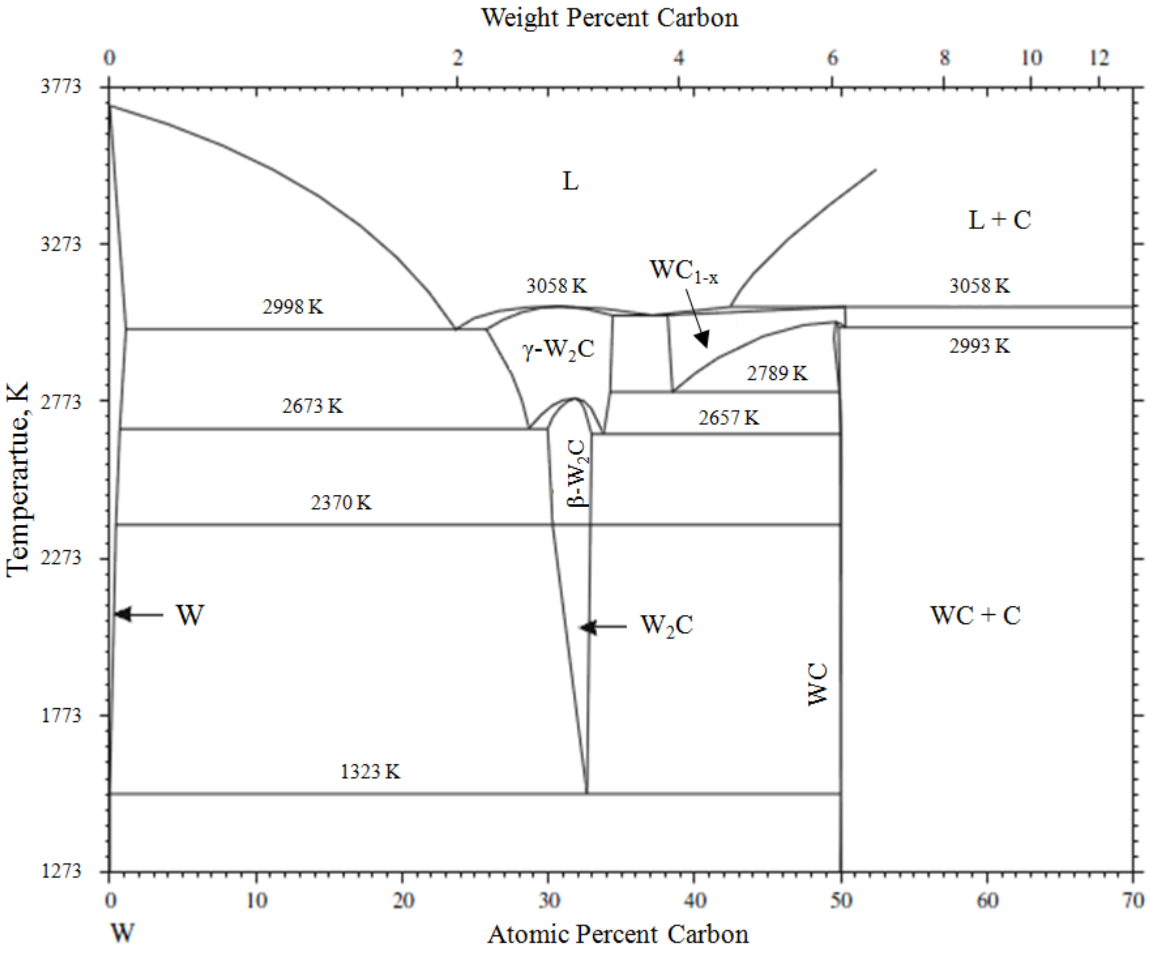

Figure 2.8: Detailed W-C phase diagram [17]. Modified by S. Jong

Table 2.1 shows the eutectic composition for each carbide phase as function of the carbon composition. From the W-C diagram and table, only WC and C are expected at Carbon concentrations higher than 60 at%. A sample containing 22 at.% tungsten or less which is then annealed up to temperatures of 2800K would only contain WC and C.

Table 2.1: Information about the carbide phases found in the W-C phase diagram dependent on the carbon concentration. The Pearson symbol for each carbon phase is shown, along with the space group symbol.

W-C crystal structure data

Phase	Composition at.% C	Pearson symbol
W	0-1	*cI2*
γ-W_2C	25.5-34	*hP3*
β-W_2C	29.5-33	*oP12*
W_2C	29.5-32.5	*hP3*
WC_{1-x}	37.1-50	*cF8*
WC	49-50	*hP2*
C	100	*hP4*

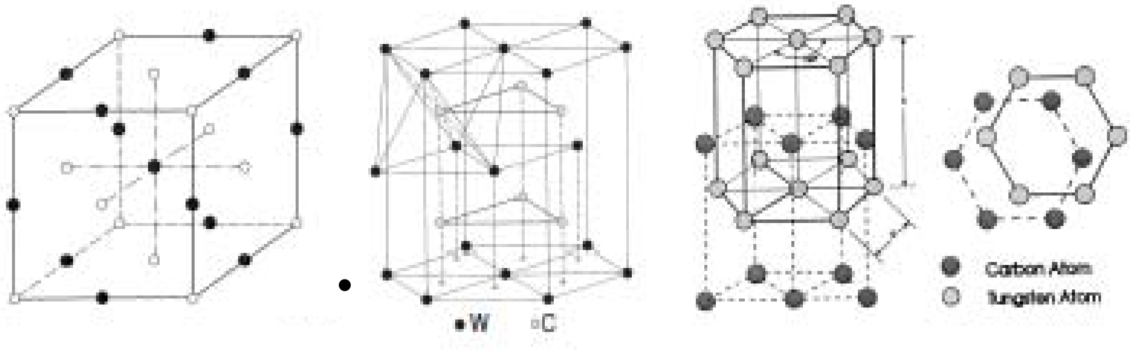

Common fcc cubic type structure. In the WC_{1-x} structure few carbon atoms are missing.

Hexagonal closed packed W_2C structure

Hexagonal stoichiometric monocarbide WC structure

Figure 2.9: Crystal structures of WC_{1-x}, W_2C and WC [3].

However, there have been reports about meta-stability in the system in both concentration- and temperature-driven non equilibrium transitions. For instance, the meta-stable WC_{1-x} and W_2C are formed as kinetic products from rapid cooling of WC. Since the sample are created by dual magnetron deposition, a non-equilibrium transitions, WC_{1-x} and W_2C can be obtained directly after sputtering or after heat treatment, as result of kinematic hindering [16].

Chapter 3

3.1 Experimental

Two different type of substrate materials, both with a dimension: 12x15 mm^2 were used to study the carbide formation of a-C:W films:

1. Polished single crystal Silicon Wafer (100).
2. Pyrolytic graphite cut parallel to basal planes and polished with diamond paste.

Both substrates were chosen for the good adhesion of the deposition and little influence during heat treatment. Before deposition, all samples were ultrasonically cleaned in isopropanol for 5 min. After cleaning in bath all samples were washed again with isopropanol, to remove any particle attached to the surface and avoid drying of isopropanol with these particles.

After cleaning the samples were placed onto a round sample holder, which could be placed in the sputtering device. The samples are located onto the sample holder as seen in figure 3.1. In the middle of the holder is a unbroken polymer-silicon coated wafer. The samples are placed equally dispersed around the silicon wafer in longitudinal direction, due to the gradient in deposition rate, hence; all samples are the same. The edge of one silicon substrate was covered with a tape to protect it from deposition. The thickness of the films could be measured afterwards with a profilometer after removing the tape. The film material was attained as a powder by inserting the coated wafer into acetone to solve the polymer.

The sample holder is placed onto a rotating disk within the sputtering device, guarantying uniform thickness and composition. The chamber was pumped overnight with a turbo molecular vacuum pump to a base pressure of $8.4 \cdot 10^{-6}\,\mathrm{Pa}$.

Figure 3.1: Sample holder after deposition, showing specimen arrangment. in the centre a coated silicon wafer around which equally disperced samples. On the right, a silicon sample where part of the sample has been taped, to determine deposited thickness.

3.2 Deposition

Two multi magnetron sputtering devices were used for depositing a-C:W films at IPP: Denton Vacuum Discovery-18 Deposition System “Denton” and Leybold Unnex 450 C “Leybold”. The power at the graphite cathode was supplied using a RF generator in the Denton device (fixed at 500W) and DC in the Leybold device (fixed at 600W). The power at the tungsten cathode, supplied using DC, was varied between 2W and 20W, depending on the concentration desired in both devices. Using DC in Leybold allowed twice as much power on the C cathode as using the RF generator, increasing deposition rate. In both devices Argon (99.999%) was used as sputtering gas.

Before deposition, the substrates were cleaned through etching for 120s at 100W using argon plasma. Etching removes the oxide layers present on the silicon substrates and enhances the adhesion. After etching, the targets are cleaned from oxide layers for 100s with closed shutters, preventing any particles falling on the substrates. After cleaning, the deposition process could begin. Liquid Nitrogen (LN_2) was used in the Denton device to reduce oxygen concentrations. No LN_2 was used during deposition in Leybold

The tungsten concentration of each deposition run was determined by Rutherford Backscattering Spectroscopy (chapter 2.2) using ^{4}He at 4MeV with a tandem accelerated in IPP. Besides the tungsten concentration, the concentration impurities of argon ($\leq 3\ at.\%$) and oxygen ($\leq 3\ at.\%$) were also measured. From the RBS spectra, tungsten concentrations from 6-30 at.% W were determined. The average film thickness was determined using the Alphastep 200 profilometer on the edge between the uncoated and coated area of the taped substrate. In table 3.1 a summary of samples deposited with concentration, carbon and tungsten power, argon flow, pre-deposition pressure, deposition time and thickness is shown.

Table 3.1: A overview of sputtered samples sorted by concentrations. The tungsten concentration displayed in the table represents the concentration of the first 100 nm of the film below the surface.

Tungsten concentration	**Deposition run name**	**Sputter device**	**C-power [W]**	**W-power [W]**	**Ar-flow [sccm]**	**Pre-Deposition Pressure [10^{-6} mbar]**	**Deposition Time [min]**	**Thick-ness [nm]**
6%	WS81	Leybold	600	4	90	0.15	300	375
7%	WS84	Leybold	600	8	90	2.5	450	930
9%	WS83	Leybold	600	6	90	0.13	1420	2550
10%	WS86	Denton	500	10	20	3.8	800	3000
12%	WS88	Denton	500	12	20	3.7	500	2200
14%	WS87	Denton	500	15	20	8.4	750	3300
18%	WS80	Leybold	600	15	90	0.16	1440	3200
22%	WS85	Leybold	500	20	90	2.3	1400	3340

After deposition, the specimens were annealed to specific temperatures: 1450K, 1800K, 2200K, 2500K and 2800K in a graphite high temperature oven (type: Labmaster very high temperature furnace, Thermal Technology Inc.) for 1h in an Argon or Helium atmosphere. For heat treatment lower than 1450K, samples were annealed for 1h in a self-made high vacuum oven (MOMO). Table 3.2 illustrate which film has received which heat treatment and was investigated by SEM.

Table 3.2: Overview of the samples who have received heat-treatment (X) and have been investigated by SEM (XXX).

Concentration W	1100K	1300K	1450K	1800K	2200K	2500K	2800K
6%			X	X	X	X	X
7%			X	X	X	X	
9%			XXX	X	XXX	XXX	XXX
10%			X	X	X	X	
12%	XXX		X	X	X	X	
14%	X	X	X	X	XXX	X	
18%	XXX	X	XXX	XXX	XXX	XXX	XXX
22%	XXX	X	XXX	X	X	X	

The crystallographic phase within the annealed a-C:W films, were examined by XRD diffraction. Carbide phases were identified by comparing peak positions within the XRD diffractogram with data from ICDD PDF. Figure 2.7 shows a diffractogram of a *θ/2θ* scan of a 22% a-C:W film annealed to 2200K. All XRD measurements were made with a Seifert XRD 3003 PTS diffractometer, using Cu *Kα* radiation. Details about the carbide phases observed in the diffractograms can be found in chapter 4, section 4.1.1.

Chapter 4

4.1 Carbide characterization

4.1.1 XRD Characterization

For the evaluation of the XRD data, all diffractograms from an annealing series have been added in a diagram for better observations of peak trends. Data regarding tungsten carbide phases from the WINPDF-file, have also been added into the diagram, making peak allocation faster and easier. Phase characterization, crystal size measurements and textures were investigated using $\theta/2\theta$ Bragg-Brentano configuration and in several cases (thin films) multi-layer/GID. The following section contains a detailed description about analyzing XRD diffractograms from all heated series. The data from the XRD diffractograms have been summarized inside an XRD tableau found in section 4.2 for a better overview.

The XRD spectrum for the annealing series of 6% a-C:W is shown in figure 4.1. This is the only series measured with the multilayer\GID configuration due to the thickness and tungsten concentration of the deposited film. In addition the diffractogram of the initial (unheated) sample has been added to act as a comparison for all other diffractograms. The initial samples of all other annealing series are similar to the 6% a-C:W, hence the initial samples have not been added into the diffractograms. For temperatures lower than 2200K, no clear carbide phases can be allocated as only broad peaks can be found. However, compared to the initial sample, few changes can be observed. A broad peak from 35° to 42° can be seen, illustrating that crystal formation has taken place. The amounts of crystallites formed are too small to be noticed. At 1800K, a small shoulder of the peak appears at 37°, indicating a possible appearance of WC_{1-x}. Heat treatment to 2200K leads to broad clear WC_{1-x} peaks at 37° and 43°, whereas there is no sign of the other carbide. A small peak around 48° is found, indicating the presence of WC, however no signs of other WC peaks around 31° and 35° were found. Heat treatment to 2500K leads to clear WC_{1-x} formation. The peaks around 37° and 43° have become narrower and no sign of WC and W_2C carbide phase can be found. The peak around 48° is still there. Within the 2800K, narrow high WC_{1-x} peaks can be found around 37° and 43° alongside with WC peaks which have appeared around 31°, 35° and 48°. Within all samples of 6% a-C:W, no W_2C phase was found. For the 2800K annealed specimen large peaks around 32-34° and 42° can be found, belonging to WO_3, which has apparently been formed during the heat cycle. As it turned out that a leak within the oven allowed oxygen to enter the purged chamber and react with the tungsten within the sample. Comparing peak intensities of WC peaks, indicate that a possible texture is present. The peak around 31° is higher than that of 36°, while the ICDD powder file suggest that the intensity of the 36° is higher. Further research has to be done to confirm texture suspicion.

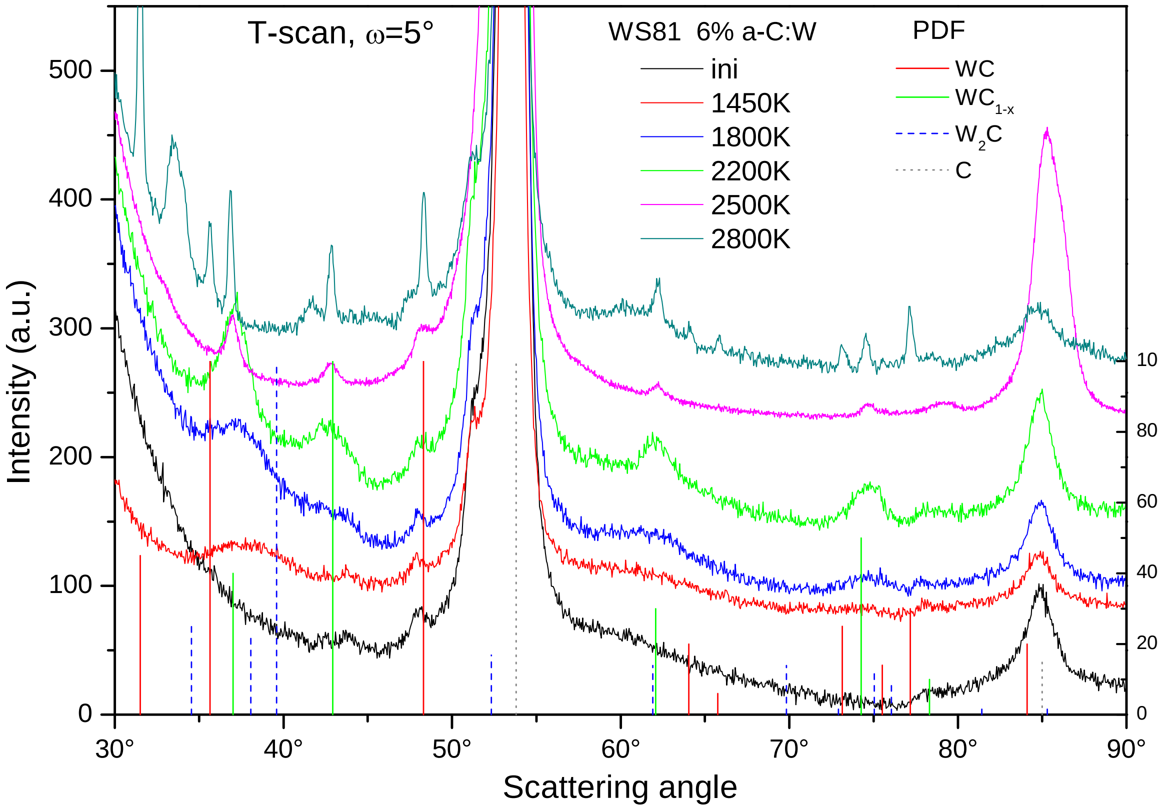

Figure 4.1: XRD diffractograms of the annealing serie of the 6% a-C:W samples.

Crystal sizes of 11 nm were measured within the 2500K specimen. For the 2800K, crystal sizes of 107 nm were measured for WC_{1-x} and >200 nm for WC. For both specimens, Bragg-Brentano setup was used for crystal size determination, i.e. narrow peaks can only be measured using this setup.

In the concentration series 6% and 7% a small peak around 48° could be found in the lower heated (1800K-2200K) specimen. At first it was believed that this peak came from the reflection of WC carbide. However, since no other WC carbide diffraction was found within the diffractogram, the peak diffraction had to come from something else. The diffractogram of an un-deposited graphite sample showed that the small peak belonged to graphite. In all other diffractograms, a small peak around 48° will be ignored until a clear WC diffraction can be allocated.

Annealing samples containing 7% and 9% a-C:W, figures 4.2 and 4.3 show identical diffractograms and carbide formation to the 6% a-C:W annealing series. These samples have been measured using $\theta/2\theta$ Bragg-Brentano configuration to obtain a better resolution for determining peak broadening by crystallite size. No clear carbide allocation can be done at temperatures below 2200K. At 2200K a small shoulder around 35° could be found in both samples, an indication for the presence of W_2C. In the 2500K specimens, WC_{1-x} has become the more dominant carbide. In the 7% 2500K diffractogram, small peaks around 34,5° and 39° can be observed, representing W_2C carbide. For the 9% 2500K a small peak can be noticed around 36°, a sign for WC. Unfortunately, the WC peak around 48° cannot be used, given that the UC graphite substrate also has a peak around the same position. For the 9% a-C:W 2800K sample WC and WC_{1-x} can be noticed. Crystal sizes of 10 nm can be measured within both 2500K specimens, whereas crystal sizes within the 9% 2800K are 104 nm for WC_{1-x} and >200 nm for WC. Both samples show no sign of texture of any kind.

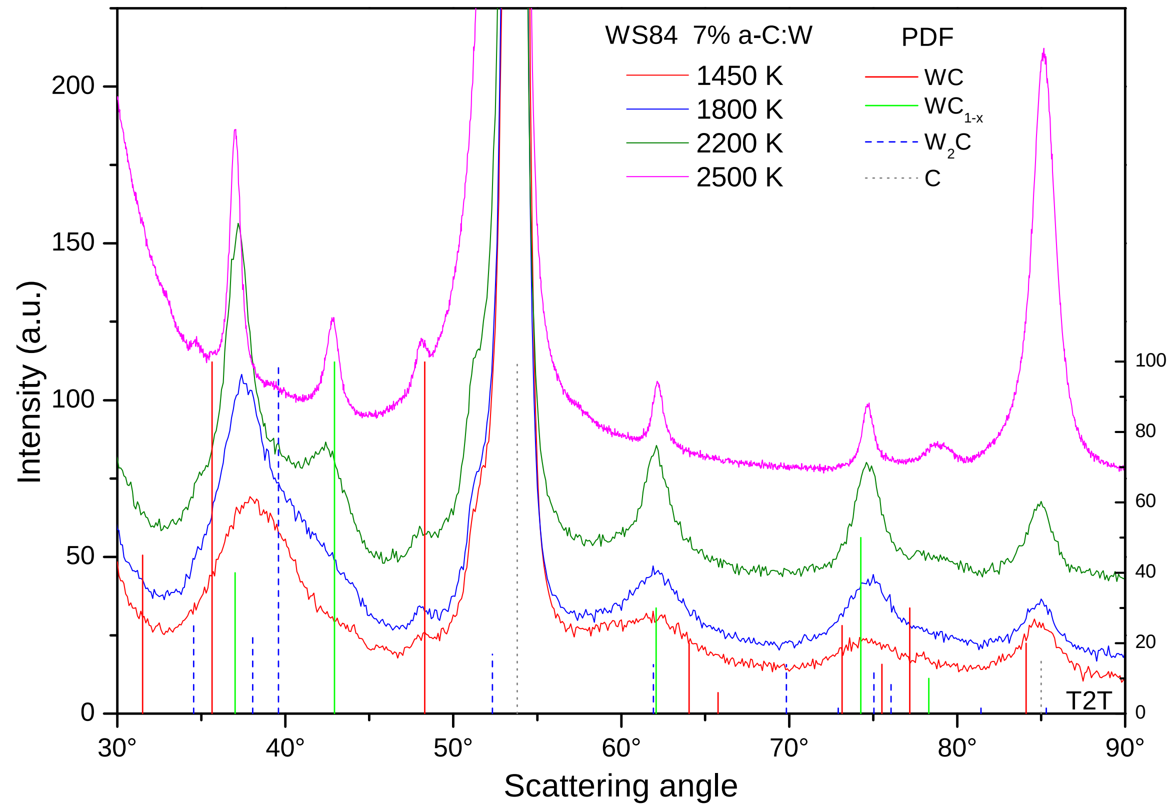

Figure 4.2: XRD diffractograms of the annealing serie of the 7% a-C:W samples.

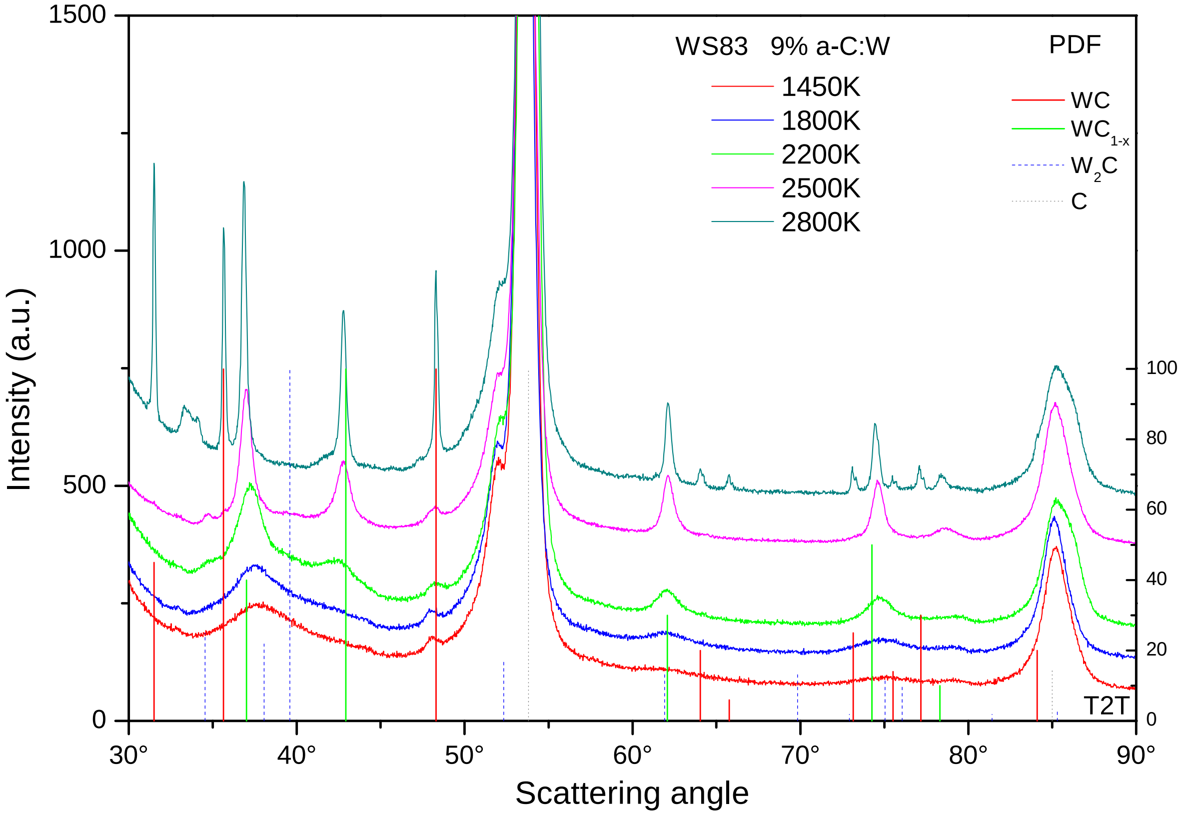

Figure 4.3: XRD diffractograms of the annealing serie of the 9% a-C:W samples.

The XRD diffractogram of a 10% a-C:W looks different to that of the 6%, 7% and 9% a-C:W, figure 4.4. For temperature up to 1800K, a large broad peak can be found around 35°- 40°, meaning small crystallites are there. Hence all three carbide have diffraction peaks in this range, therefore no assumption about individual crystal carbides can be made. The broad peak shows two shoulders, one on each side. The shoulder on the left side is found around 35°, an indication for W_2C, where the shoulder on the right side can be found near 39°, another indication for W_2C. Although all anomalies indicate the presents of W_2C, small amounts of WC and WC_{1-x} might be present. Annealing to 2200K clearly leads to the formation of W_2C peaks at 34°, 38° and 39°. A small shoulder of the 39° peak can be noticed, indicating the presence of $WC_{1-x.}$ In the 2500K specimen large peaks appear which were not present in the lower annealed samples belonging to WC, while the WC_{1-x} strongly increase in intensity. A close observation shows that the intensity of the W_2C peaks has declined, meaning that the W_2C is slowly disappearing. Crystal measurement for the 2500K sample show that the WC_{1-x} crystals are 10 nm big, WC crystals 27 nm, and W_2C are smaller than 5 nm. Unfortunately no 2800K sample is available, hence no conclusion can be drawn whether W_2C has completely disappeared or is still present.

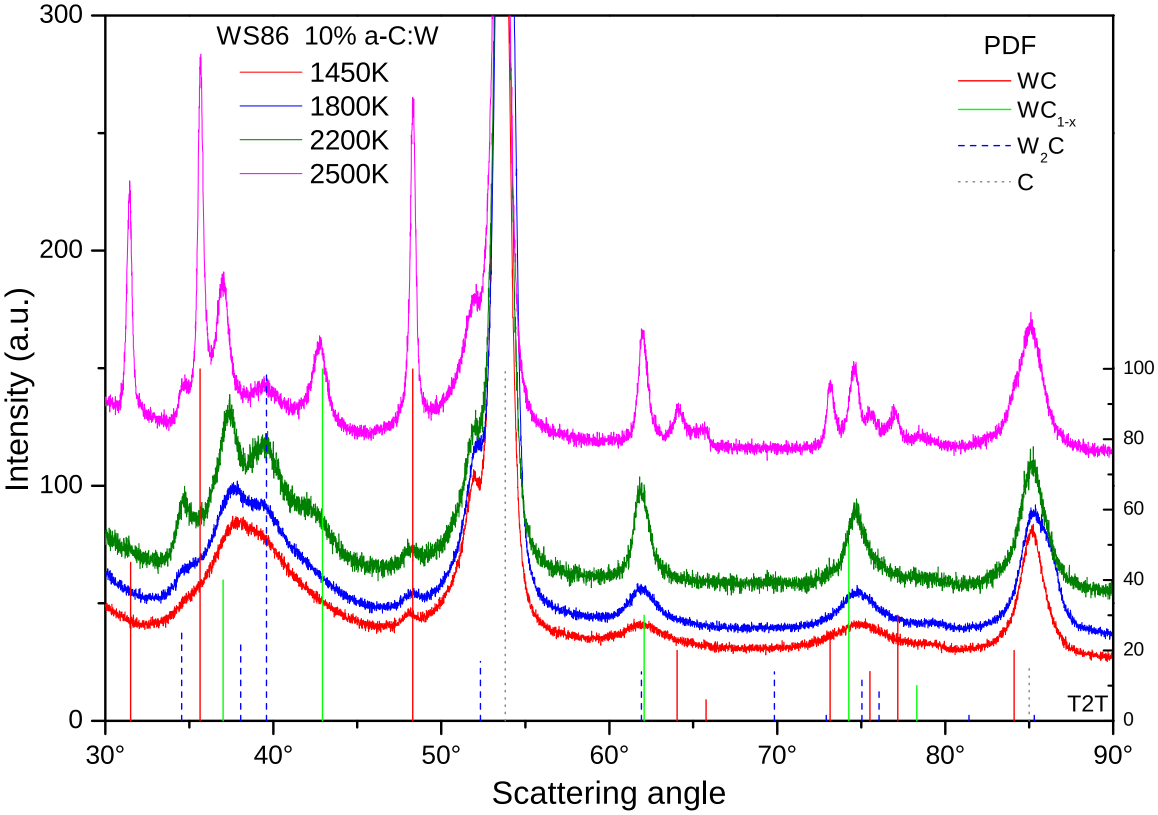

Figure 4.4: XRD diffractograms of the annealing serie of the 10% a-C:W samples.

In the 12% a-C:W, figure 4.5, no clear carbide formation is observed at 1450K. At 1800K small narrow WC peaks, can be found around 31° and 35°. A large broad peak can be observed from 35° - 40° with 2 peaks on the shoulder. These peaks indicate the presence of W_2C. In the 2200K clear W_2C peaks can be noticed around 38° and 39°, whereas the shape of the WC peaks has not changed. At 2500K, high and narrow WC peaks can be found around 31°, 35° and 48°, a sign for large crystals within this specimen. The intensity of the W_2C peaks seem to decrease compared to the 2200K specimen. A peak on the shoulder around 43° can be seen, which is clearly a sign of $WC_{1-x.}$ Unfortunately, no annealing to 2800K was done, therefore no conclusion about the disappearing of W2C and appearing of WC_{1-x} can be made. Crystal sizes of 8 nm for W_2C and 30 nm for WC were measured for the 1800K specimen. Both average crystal sizes have increased for the 2200K specimen: 12 nm for W_2C and 42 nm for WC. Crystal measurements for the 2500K show that average crystal sizes for WC_{1-x} are 11 nm big, W_2C are smaller than 5 nm and WC are 35 nm.

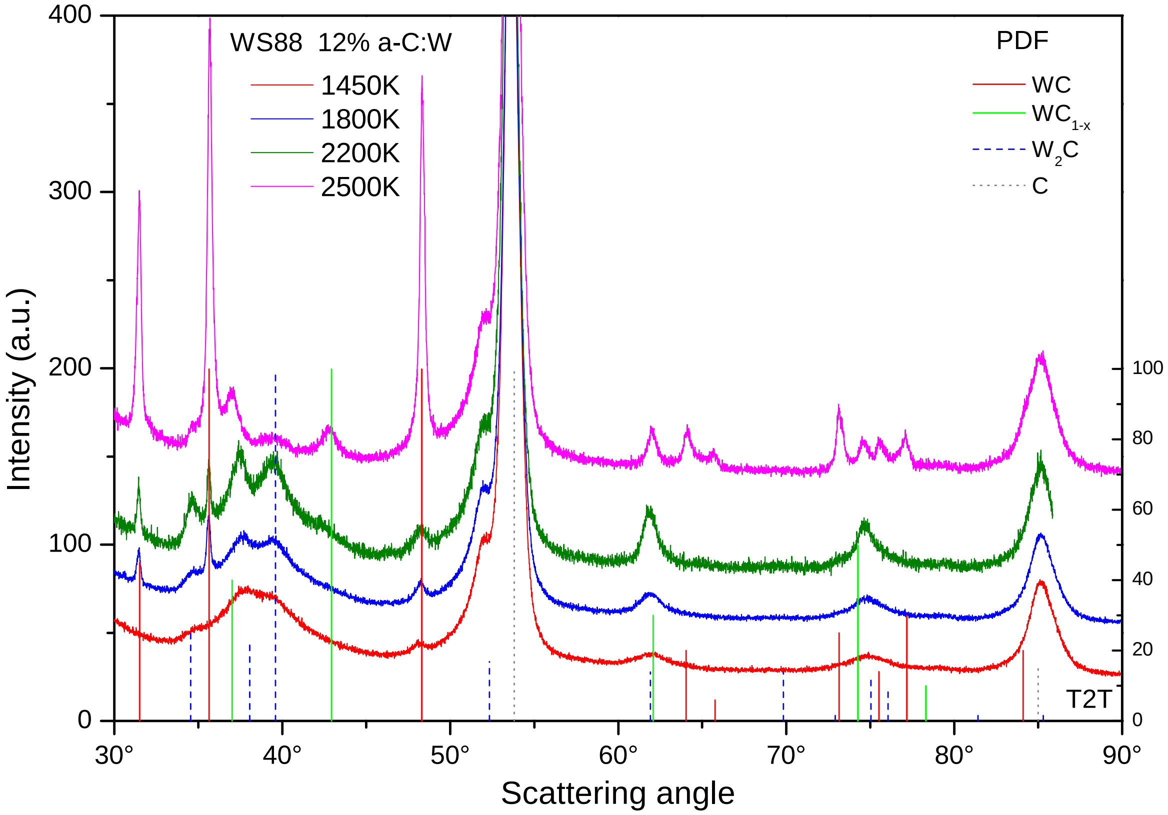

Figure 4.5: XRD diffractograms of the annealing serie of the 12% a-C:W samples.

In the 14% a-C:W, figure 4.6, clear W_2C carbide formation around 37° and 39° is seen at 1450K. In addition small peaks appear near 31° and 36°, an indication for WC. At 1800K and 2200K, clear narrow WC carbide peaks can be seen alongside W_2C. The 2500K specimen only contains WC, as no signs of W_2C peaks are found. W_2C has completely disappeared. For the first time, WC is the only phase found within a sample. In all lower tungsten concentrated samples, WC was found alongside W_2C or WC_{1-x} and was recessive compared to W_2C and WC_{1-x}.

Crystal sizes of 8 nm can be measured for W_2C at 1450K and 1800K. At 2200K, 16 nm crystals for W_2C are measured. The WC peak in the 1450K specimen, indicate that the WC crystals are very small (< 5nm). At 1800K, the WC crystals have grown to an average size of 19 nm. At 2200K, 62 nm crystal are measured, while in the 2500K, actual crystal size (>100 nm) could not be measured due to instrumental broadening.

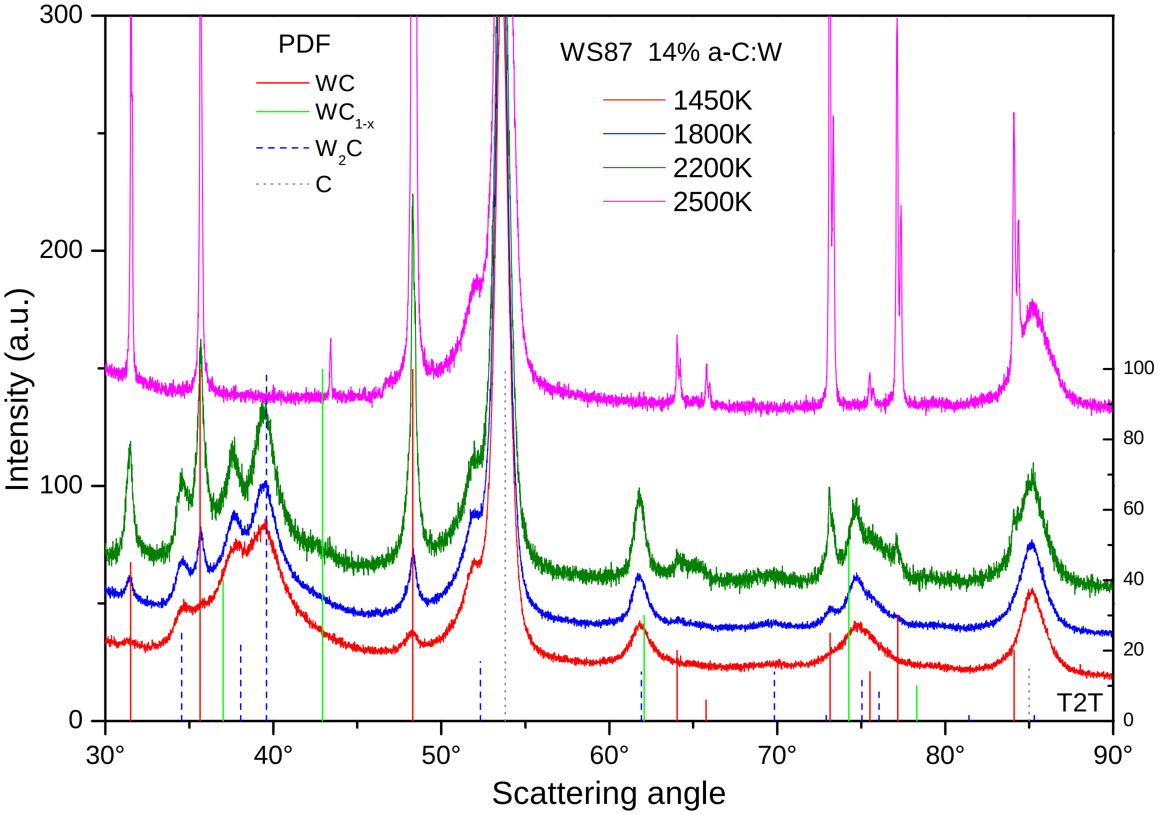

Figure 4.6: XRD diffractograms of the annealing serie of the 14% a-C:W samples.

The 18%, figure 4.7, contains a mixture of W_2C and WC, where the ratio WC to W2C is increased to WC for temperatures up to 2200K. At 2500K, the majority of W_2C has disappeared, and large WC peaks are observed. The peak around 37° in the 2500K indicates that W_2C is still present; however none of the other W_2C diffraction peaks can be noticed with the spectrum. Even if small quantities of W_2C are left, due to the strong tungsten gradient within the sample, no clear explanation can be given to why only the 37° peak appears within the spectrum. Therefore this artifact will be disregarded during evaluations in this work.

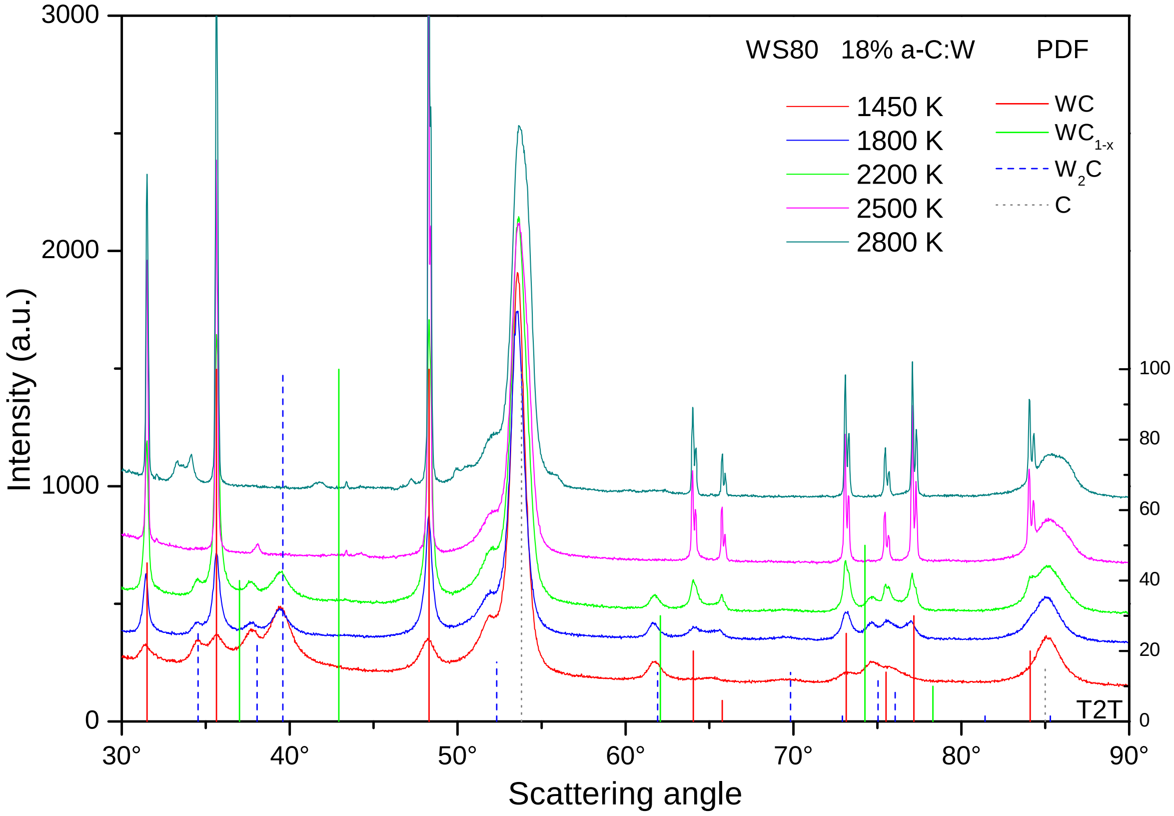

Figure 4.7: XRD diffractograms of the annealing serie of the 18% a-C:W samples.

The 22% a-C:W sample, figure 4.8, shows two particular interesting features. As initially suspected, the only carbide found within the heat series of 1450K up to 2800K is WC. The diffractograms show high narrow peaks, indicating large crystallites. The second feature is the peaks around 43°. These sharp peaks cannot be found within the WINPDF database, and are therefore un-allocatable. It could be suggested, that this peak belongs to an unknown WC crystal phase. the peak is also observed within the 14% 2500K series. In addition the peak intensity is only 1% of the intensity of the 37° peak, therefore only observable for thick layers and if no WC_{1-x} phase is present. It was believed that annealing this series to lower temperatures 1100K – 1300K might show the formation of the other carbides. Unfortunately, the spectrum of the 1100K and 1300K sample showed no signal only broad peak. These samples were amorphous.

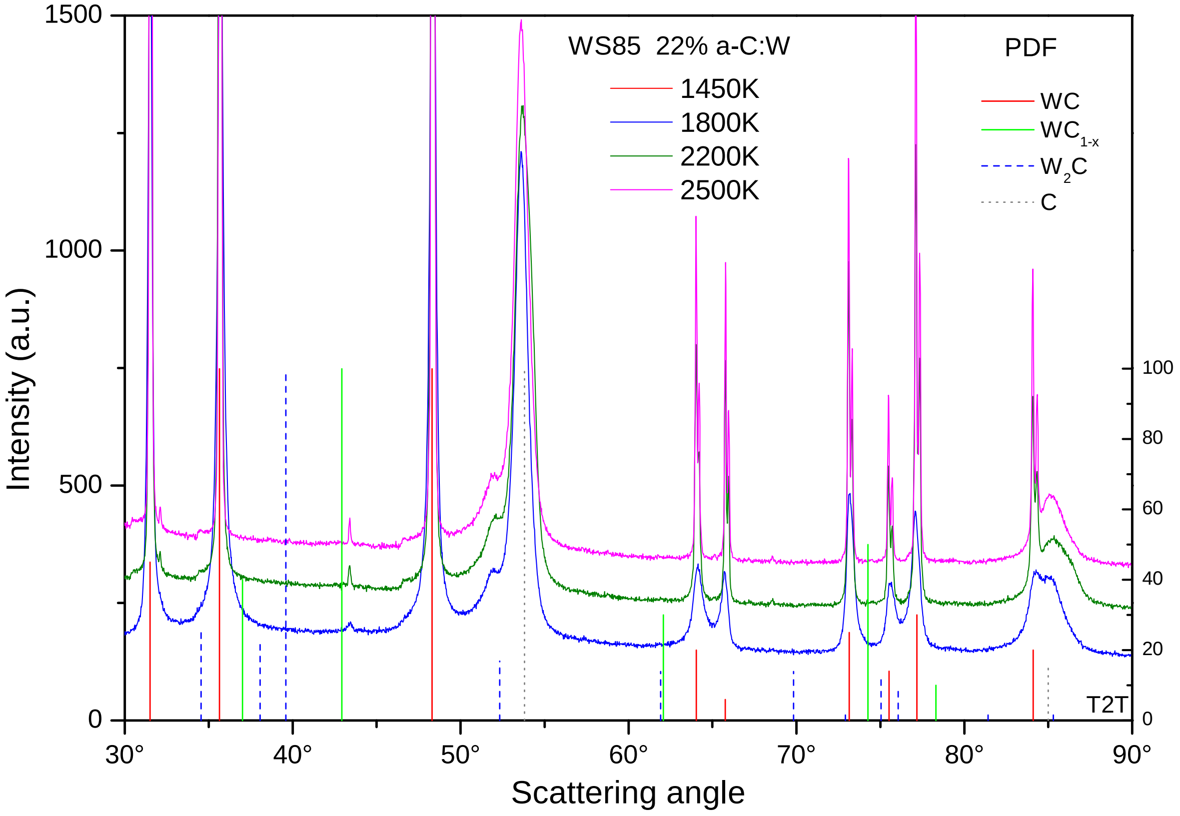

Figure 4.8: XRD diffractograms of the annealing serie of the 22% a-C:W samples.

4.1.2 SEM

For surface and sub-surface morphology analysis and for comparison of crystal size, the sample was investigated under a SEM (Helios Nanolab 600, FEI), allowing to make cross-sections within the sample (section 2.3). Figure 4.9 shows the surface morphology and cross-section from 9% and 18% a-C:W annealed to 2800K. The surface of the 9% films contains a broad distribution of black anomalies on the a-C:W surface. Within the 9% film, a distribution of crystal sizes is visible (large crystallites: 0.2–2 µm in size, small crystallites: 10–100 nm in size) and found through the sample, where the large crystallites can only be found underneath the black anomalies on the surface. The surface of the 18% film is rougher than the 9% film. A cross-section of the 18% film shows that huge tungsten carbide crystals (white) have been build. The black area is amorphous tungsten. A closer look at the sample reveals that the coating is peeling off.

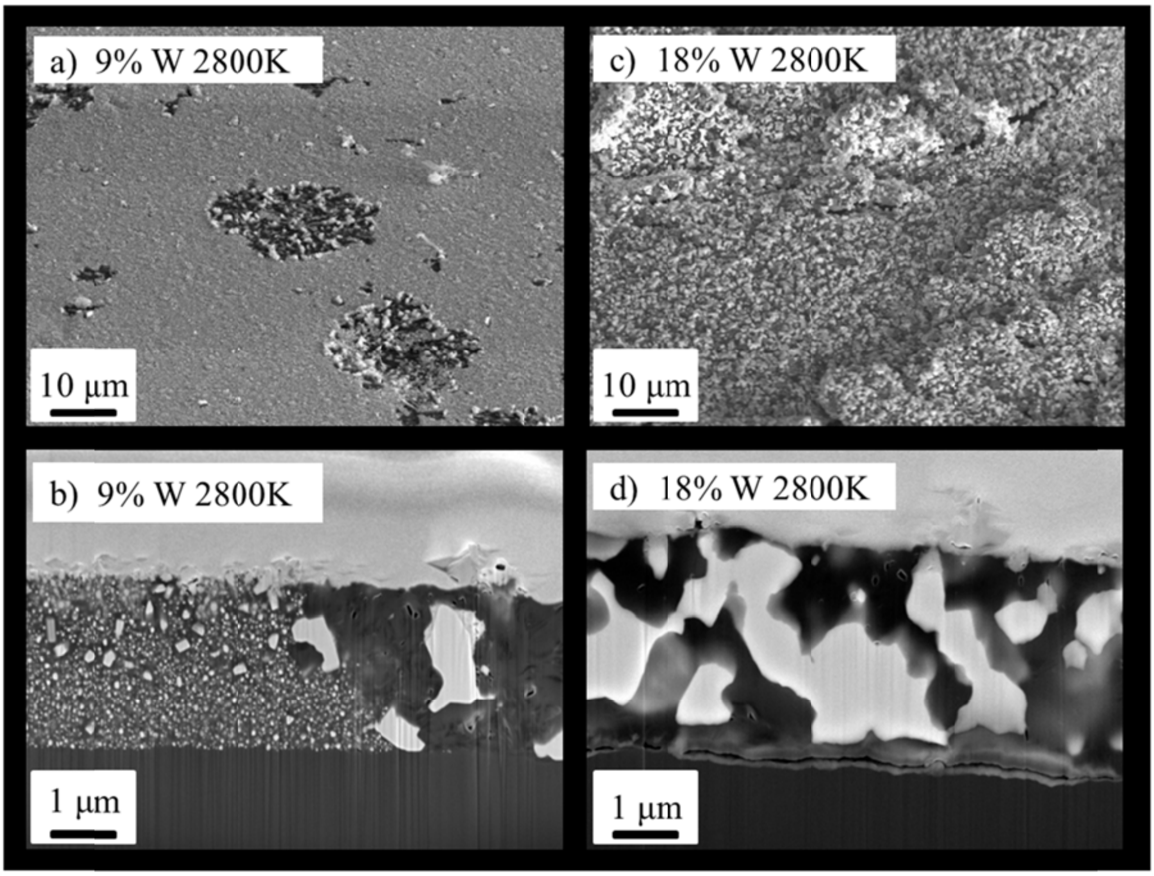

Figure 4.9: SEM from a 2800K a-C:W film. a) surface morphology of a 9% a-c:W film. b) SEM cross-section of a 9% a-C:W film. c) surface morphology of a 18% a-C:W film. d) SEM cross-section of a 18% a-c:W film.

The origin of the black spots may be result of impurities formed during deposition or heat treatment. Hence many factors could influence this behavior; no further investigation was done concerning the origin of these anomalies. Other samples were investigated to see if a binomial distribution were presence, like in the 2800K 9% a-C:W film.

Figure 4.10a and b show a SEM cross-section of a-C:W films annealed to 2200K, with 9% and 18% tungsten concentration. The 9% tungsten sample shows very small crystallites (1-10 nm) distributed uniformly throughout the layer. Throughout the 18% tungsten sample a wide distribution of crystal sizes can be observed, ranging from 10–200 nm as function of depth. The crystal size increases in average size with increasing distance from the substrate. The origin for this unique behavior will be discussed in section 4.2.2.

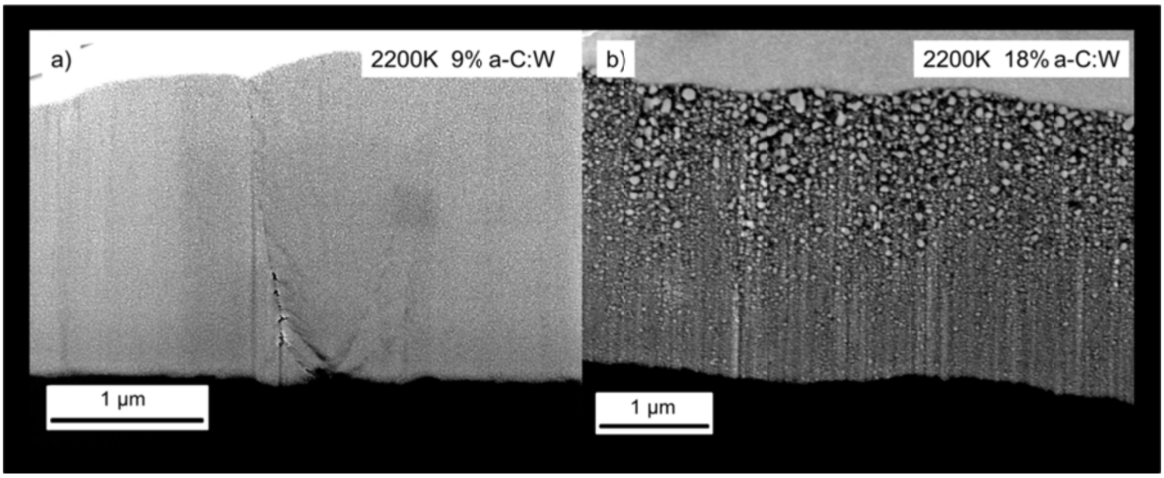

Figure 4.10: SEM cross-sections from a 2200K a-C:W film. a) 9% a-C:W. b) 18% a-C:W

Figure 4.11 shows a SEM cross-section of a-C:W films annealed to 1450K, with 18% and 22% W concentration. The 18% a-C:W film contains very small crystallite, homogenoues distributed throughout the sample (5-50 nm). The 22% a-C:W film contains crystals (50-300 nm) that are orientated in vertical direction, an indication for texture. Inside the deposited layers, nano-shaped structures (black lines) are found. In addition the coating appears to peal off by destroying the graphite substrate, as can be seen by black empty pores in the graphite substrate.

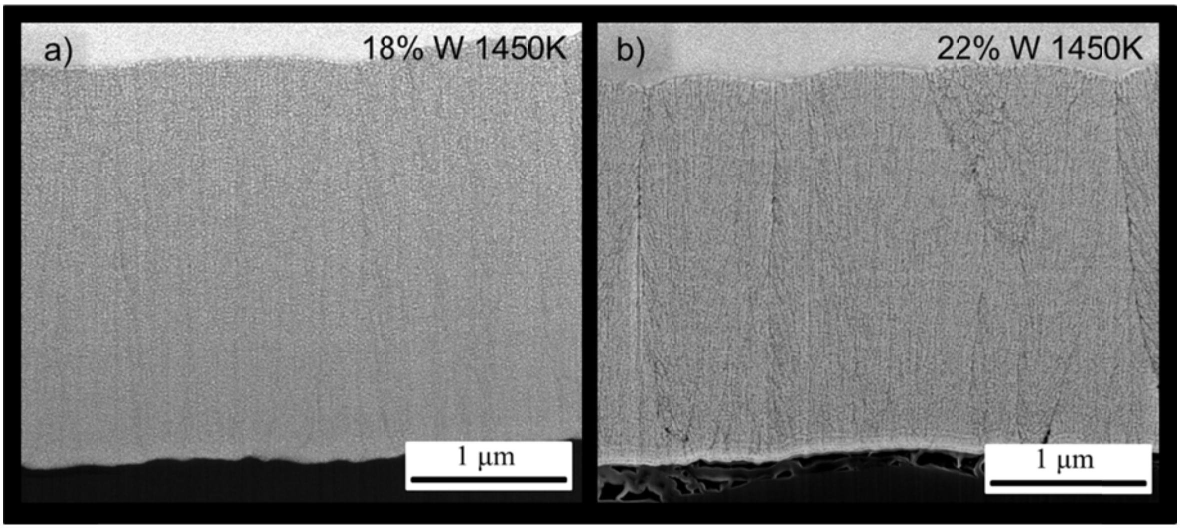

Figure 4.11: SEM cross-sections from a 2200K a-C:W film. a) 18% a-C:W. b) 22% a-C:W.

4.1.3 Nano-diffraction

From the XRD diffraction pattern of the 1450K 9% a-C:W, no clear carbide phase was allocatable. For individual phase identification of nano structures and confirmation of cross-section, the sample was sent to Warsaw. There characterization with a high resolution STEM on a thin lamella cut from the sample (Hitachi HD-2700) was done. This microscope is able to image crystals up to atomic size (<1 nm). Furthermore, nano-diffraction on an area of several nm^2 can be performed which allows to distinguish the different tungsten carbide phases form each other. Also formation of graphite in the amorphous carbon matrix can be detected. The findings and results from nano diffraction done on several samples can be found in [18] [19] and will be used to support XRD and SEM findings in section 4.2

4.2 XRD and SEM Tableau

All the data from section 4.1, XRD, SEM and nano-diffraction have been summarized into two tableaus. The results from the XRD-diffractograms; carbide phases and crystal sizes have been summarized into the first tableau (4.12). The results from SEM and nano-diffraction have been summarized in the second tableau. Both tableaus have the same layout, where the sample is expressed by temperature, x-axis, and tungsten concentration, y-axis.

To express specific information colors have been added. Yellow, blue and green represent the carbides WC, W_2C and WC_{1-x}, respectively. Besides these colors, white, dark grey and violet are used: white is used to symbolize samples that have not yet been annealed nor researched. Dark grey is used for initial samples and for annealed samples which have a diffractogram very similar to initial ones. Violet is used for samples which have small crystallites, but which are too small for interpolation. These samples however differ from the initial samples. In some samples a combination of violet and a carbide color can be observed. These samples still have broad peaks, small crystallites, but tend to shift towards a single phase. it is assumed that the majority of the crystallites belong to this carbide, however other carbides might still be present.

4.2.1 XRD Phase analysis

When looking at the XRD tableau generally, we suspected for the thermo dynamic phase diagram (figure 2.8) the entire tableau to be in yellow (WC). As discussed in section 2.5 the only carbide phase that exists within samples with a tungsten concentration of 6%-25%, annealed to temperatures from room temperature up to 2800K is WC. However, WC is only mainly found within the higher concentrated and annealed films. Besides the suspected WC, also W_2C and WC_{1-x} can be found within the lower concentrated films. WC_{1-x} is observed in the low concentrated a-C:W films, whereas W_2C is present in the intermediate concentrated a-C:W films. Besides the presence of all three carbides within the tableau, most of the samples contain a mixture of two carbides. From all specimen containing a mixture of crystallites, WC is always one of them. Only the low concentrated samples contain a mixture of WC and WC_{1-x} after heat treatment to 2800K. All other samples contain a mixture of WC and W_2C. Unlike with WC_{1-x}, these mixed samples only appear after heat treatment from 1450K up to 2200K. Above 2200K, no more W_2C is present, only WC.

The disappearing of W_2C can be explained by the fact that W_2C is a transit-phase for WC as is discussed in the thesis of Jens Luthin. Both carbides have a hexagonal structure and WC is thermodynamically the most stable carbide. However, this does not define the formation of W_2C, whose building enthalpy is higher than that of WC. In addition, the transport of tungsten necessary to build W_2C requires more energy than that of carbon.

The formation of WC_{1-x} in the lower concentrated films 6-9 at.% W is very remarkable. WC_{1-x} is known to be thermodynamically stable around temperatures of 1500K-2800K and at tungsten concentration levels of 50-62.9 at.% (figure 2.8). However in our case, WC_{1-x} can be found around concentration levels of 6-10% and from 2200K up to 2800K. Nevertheless, since XRD is our primary characterization method, it could be possible that WC_{1-x} exists at lower temperatures but is not detected. The formation of WC_{1-x} seems strange due to the redundant amount of carbon present and that the building enthalpy of WC is lower, making it more thermodynamically stable. This would make a combination of both carbides more reasonable than just finding WC_{1-x} in the annealed samples. In the 2800K samples, both WC and WC_{1-x} can be spotted. Another interesting fact is that within the annealed samples of 1100K and 1300K, no clear carbide formation was found. The mobility in atoms in these films seems to be too low at these temperatures.

Comparing the crystallite sizes of the W_2C phase in all samples shows that the maximum crystal size does not exceed 20 nm. All samples which contain W_2C have small crystal sizes, meaning that W_2C can be considered to be meta-stable, in non-thermodynamic state. The maximum size of WC_{1-x} crystals are larger than 60 nm, whereas the maximum size of WC crystals cannot be determined using XRD-methods, but are larger than 100nm.

XRD Tableau (next page): The elements within the XRD Tableau have been divided into two sections. The left section, illustrates which carbide can be observed within the sample. Furthermore, it tells about the abundance of each carbide phase by comparing their peak intensities by the area fraction. The right section, divided into 3 rows where each row represents one of three carbides, gives us information about the grain sizes. The height of the row informs us about the average crystal size of the respective carbide within the sample calculated with the Scherrer equation (2.3). In the left upper corner of the tableau, a color index for is shown. On the right side of the Tableau two lines illustrate where which grain size is found. The grain sizes scale is divided into following sizes (from bottom to top): < 5, 5, 10, 20, 30, 40, 50, 60, 70, 80, 100 and 200 nm. At the bottom of each row, the average crystal size is given for better comparison. No textures were interpreted from any diffractogram during this research.

SEM tableau (page 45): The elements in SEM/STEM tableau are also divided into two sections. The left section contains information acquired from nano-diffraction in Warsaw and gives us information about the carbide phases located within the sample as well as abundance. From the lamella, small crystallites were randomly chosen on which then nano-diffraction was performed. The right section is a schematic drawing of crystal sizes and size distribution acquired from SEM. The height of each row is a rough estimate symbolizing the quantity of crystals numbers in that size range in the sample. Both scales have been plotted in a roughly logarithmic scale, so that all sizes can be plotted. The scale used for the crystal sizes (from left to right) is divided into: 1, 2, 5, 7, 10, 20, 50, 100, 200, 500, 1000 and 2000nm. In the left upper corner a color index is illustrated. Two lines near the 2500K 18% sample, demonstrate where the next range begins.

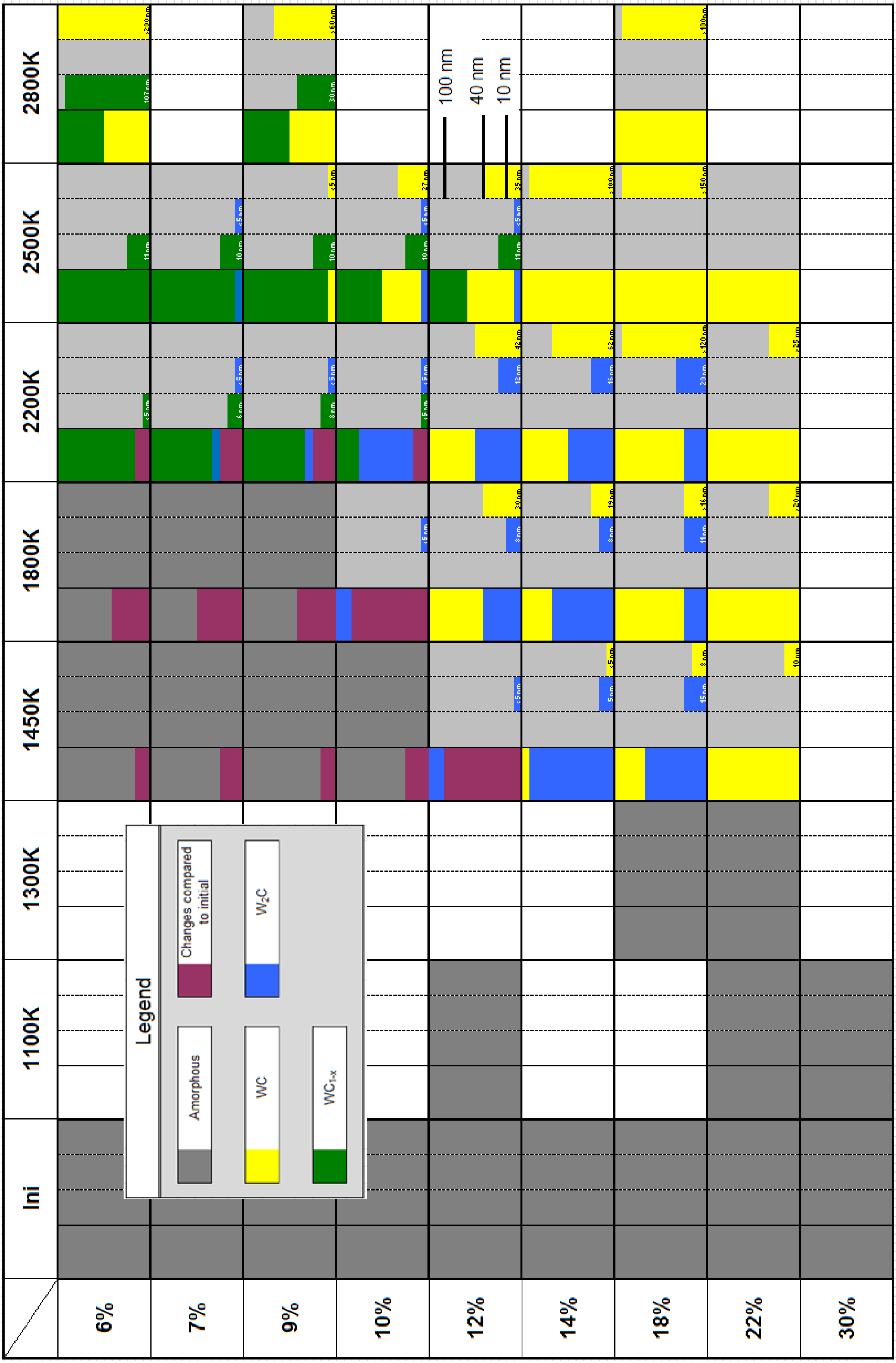

Figure 4.12: XRD tableau. Figure caption is on the previous page

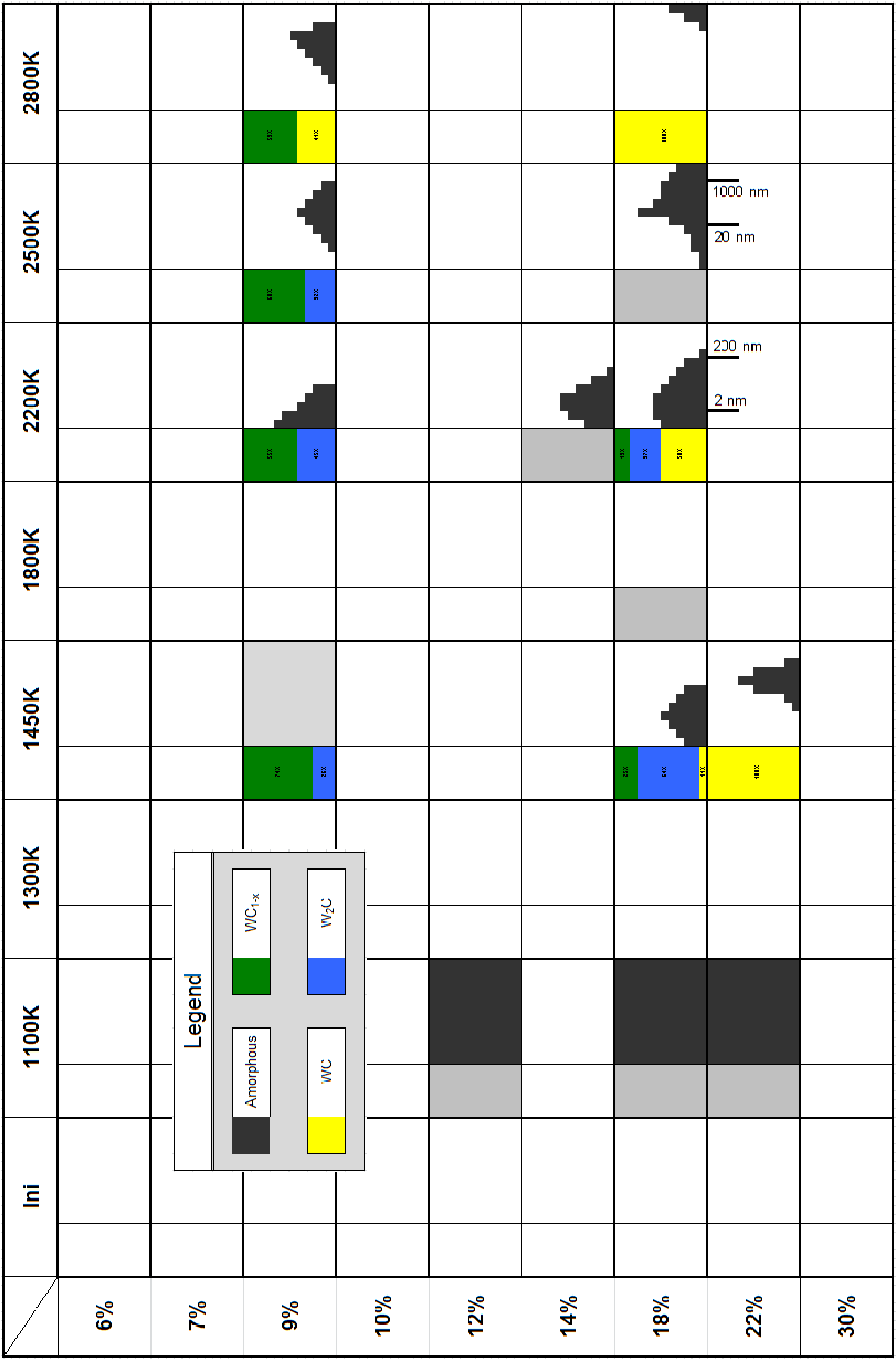

Figure 4.13: SEM & nano-diffraction tableau. Figure caption is on the previous page

4.2.2 SEM

SEM cross-sections show that the crystal sizes grow with increasing temperatures for the 9% and 18% a-C:W films. In addition to observing crystal growth, crystal size distribution is given and fast crystal size comparison to other samples and to the XRD findings (4.12) is allowed by the SEM tableau (4.13). In general the crystal sizes measured by XRD correspond to the findings of SEM. With SEM also crystal sizes above the detection limit of XRD, bounded instrumental broadening, are determined. XRD limitation indicated that the crystal sizes were larger than 100 nm, whereas SEM found crystal sizes of 1 μm. Besides crystal size limitation, the XRD cannot distinguish binomial crystal distribution properly as seen in the 9% a-C:W 2800K. It must be noted that the crystal sizes and distribution in the SEM tableau are a rough schematic drawing, as realistic image analysis cannot be done or is difficult.

Furthermore, the SEM tableau reveals increasing crystal sizes with increasing concentration at specific temperatures. At a certain temperature and tungsten concentration this rapid crystal growth is noticeable. At 2200K the 18% a-C:W film (figure 4.10b) shows that the crystal size depends on the tungsten concentration (14-18 at.%). To confirm that this crystal size gradient was result from a concentration gradient found within the sample (figure 2.3), special designed multi-layers were produced by magnetron sputtering. These multi-layers, each layer with a different tungsten concentration, should confirm that the crystal size gradient within the 18% a-C:W sample was caused by the concentration differences and exclude other factors (e.g. oxygen, substrate).

Figure 4.14 shows the RBS spectrum of the special multi-layer produced to investigate the crystal size gradient. The sample is build-up out of two protective carbon coatings, which should protect the a-C:W deposition from outside influences, i.e. the substrate and oxygen from the surface. Inside the sample, seven stacked a-C:W films each with different tungsten concentration, have been deposited on top of each other. On the top is a 25% a-C:W coating, with underneath a 13,5% a-C:W coating. The other five coating are respectively: 16, 18.7 20.7, 22.3, 24 at.% tungsten. After heat treatment, it is expected that within each layer different crystal sizes were found. This multilayer represents an artificial concentration gradient, which after heat treatment should result in a crystal size gradient.

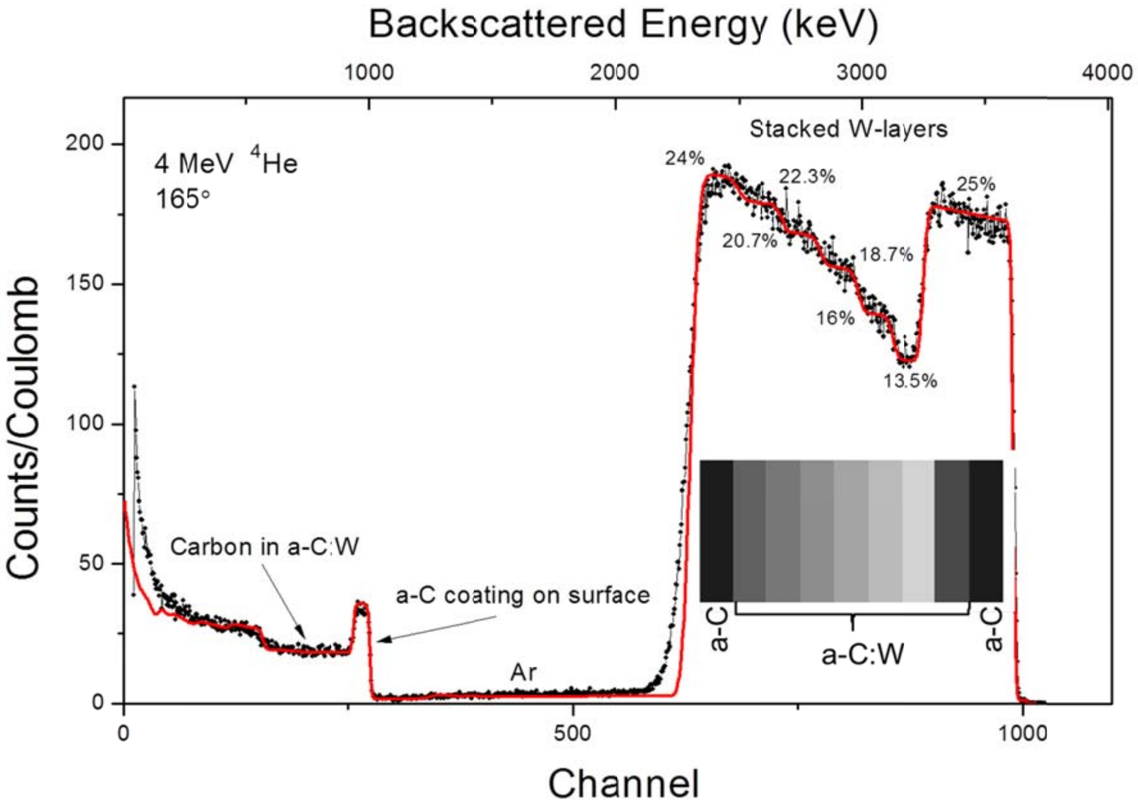

Figure 4.14: RBS spectrum of a special designed multi-layer to investigate crystal size gradient behavior. Seven stacked tungsten layers within the spectrum vary in tungsten concentration.

Figure 4.15 shows the cross-section of the experimental crystal size gradient and simulated crystal size gradient after heat treatment to 2200K. Within figure 4.15a, the crystal size decreases as function of depth, whereas the crystal sizes within figure 4.15b have steps. Heat treatment of the multi-layers proves that the crystal size depends on the tungsten concentration within the sample.

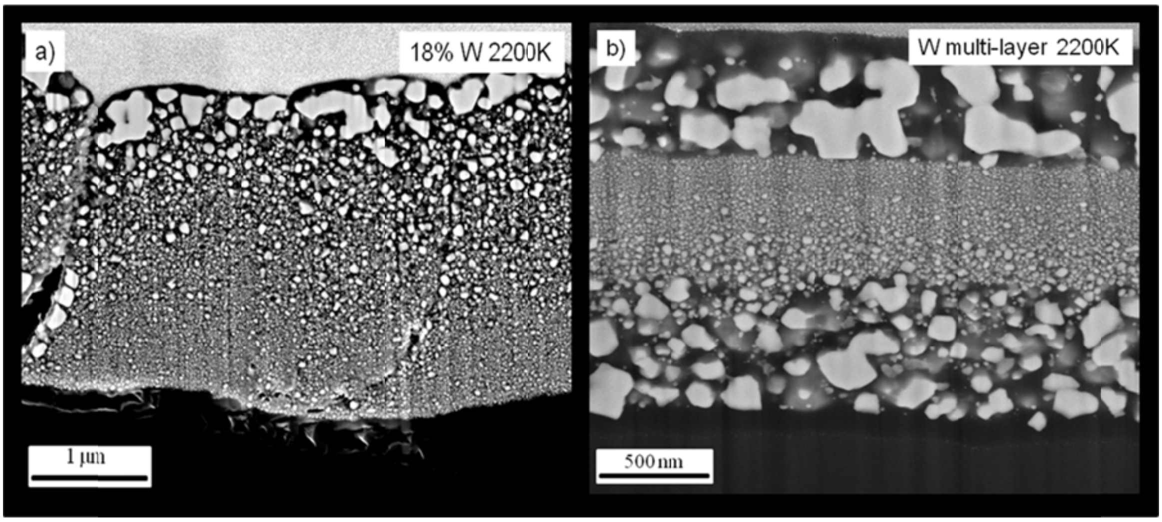

Figure 4.15: SEM cross-sections from 2200K a-C:W films. a) experimental crystal size gradient found within the 18% a-C:W film. b) artificial crystal size gradient by depositing 7 a-c:W coating with different concentrations between two carbon coating on a film.

4.2.3 Nano-diffraction

Although nano-diffraction initially only acted for comparison to the results from XRD, the results show some interesting new findings. Within the 9% a-C:W sample, a mixture of both W_2C and WC_{1-x} is found in the 1450K, 2200K and 2500K. Within the 2800K a mixture of WC_{1-x} and WC is found. These findings are in contradict to the XRD findings, which concluded that within the 2200K and 2500K only WC_{1-x} is present. In addition, the XRD diffractogram of 1450K showed no clear crystal morphology, except wide peaks, meaning no conclusion about the carbide phases could be made. With nano-diffraction, phase identification of W_2C, WC_{1-x} and WC crystallites of nm size could be done. Besides phase analysis, crystal size analysis of very small crystallites (1-5 nm) can be done.

Besides the 9% a-C:W film, nano diffraction was also done on samples from 18% a-C:W and 22% a-C:W. The findings from the 22% a-C:W support the XRD findings as only WC was found. Besides phase identification on nm-levels, bright and dark field imaging illustrate that within the 22% W sample, clearly WC and graphite has formed. The findings done on the 18% a-C:W film were surprising. Within the 1450K and 2200K, all three carbide phases: WC, W_2C and WC_{1-x} were found, figure 4.16 and 4.17. Within the 1450K sample, the majority of the crystals are W_2C, whereas a few are WC and WC_{1-x}.

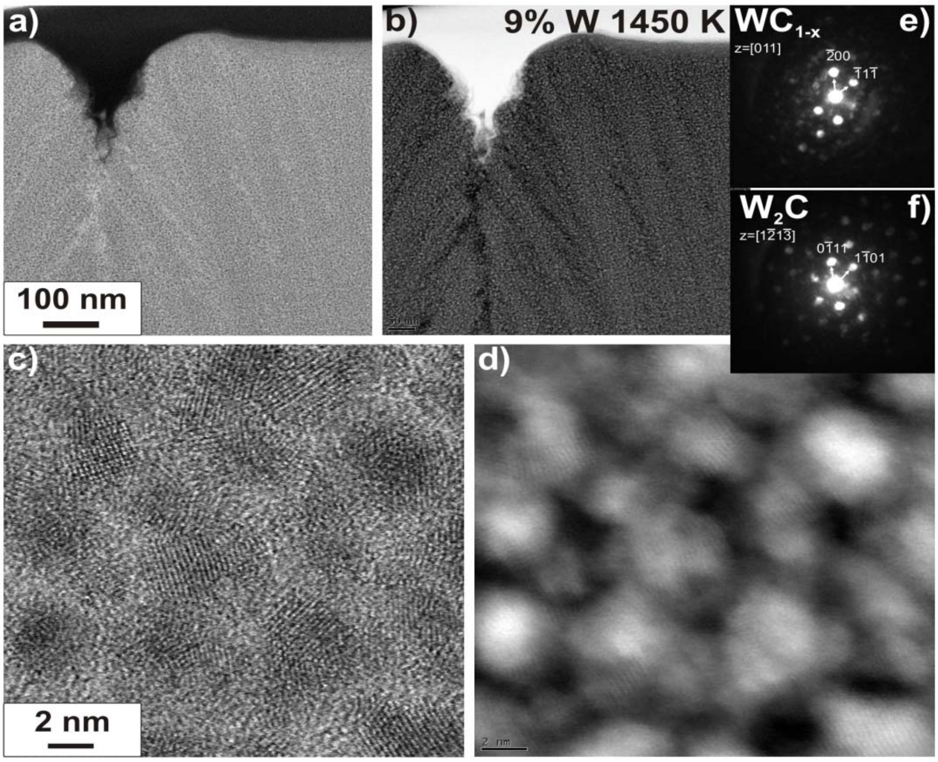

Fig. 4.15. STEM images in bright field mode (a,c) and in Z-contrast (b,d) together with typical electron diffractograms of WC_{1-x} (e) and W_2C (f) of 9% W film annealed at 1450K [18].

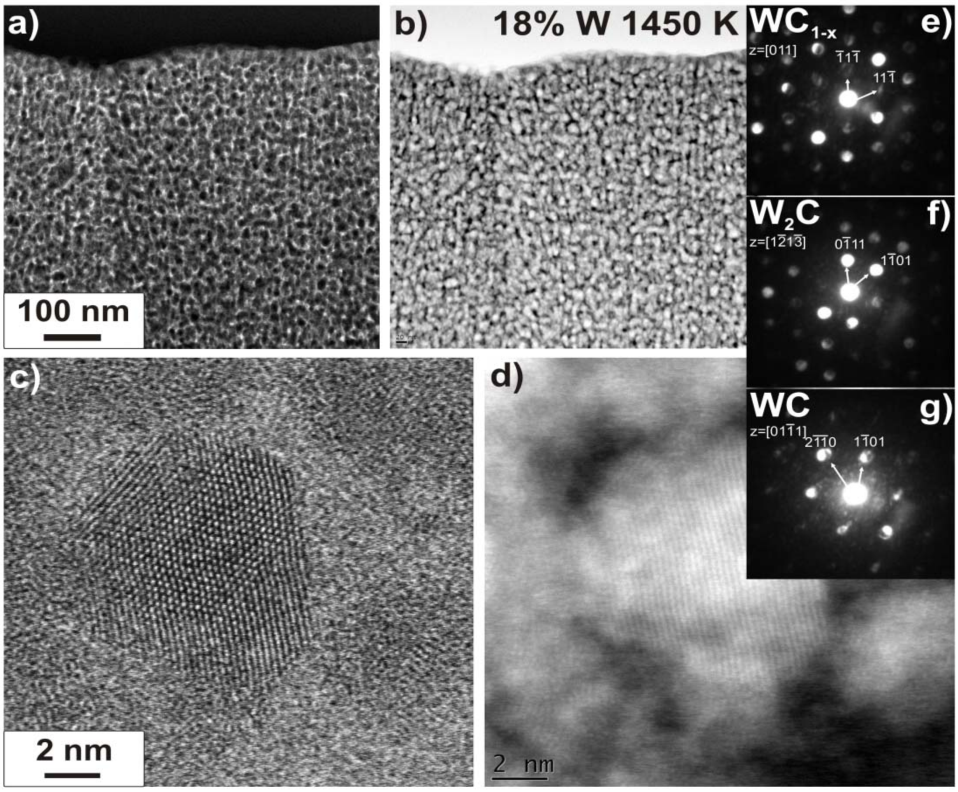

Fig. 4.16. STEM images in BF mode (a,c) and in Z-contrast (b,d) together with typical electron diffractograms of WC_{1-x} (e) W_2C (f) and WC (g) of 18% W film annealed at 1450K [18].

In the 2200K, the majority of the crystals belong to WC, whereas the amount of W_2C has reduced. The amount of WC_{1-x} found in both samples does not vary much during both heat intervals. The small amount of WC_{1-x} found clarifies the reason WC_{1-x} is not found within the XRD diffractogram. Within the 2800K sample, both W_2C and WC_{1-x} have disappeared and changed into WC.

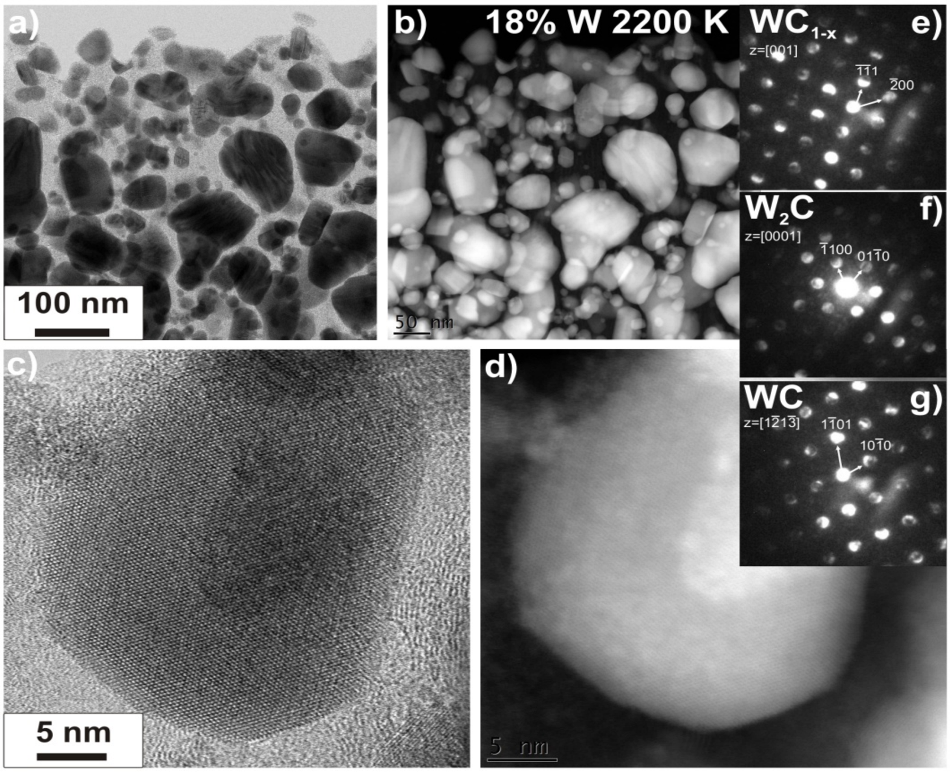

Fig. 4.17. STEM images in BF mode (a,c) and in Z-contrast (b,d) together with typical electron diffractograms of WC_{1-x} (e) W_2C (f) and WC (g) of 18% W film annealed at 2200K [18].

The reason for the appearance of all three carbide may be the result of a concentration gradient found within the sample (figure 4.10b). Further research is still done on this sample. A hypothesis is that the WC_{1-x} is found in the lower concentrated part of the sample, in the middle a mixture of W_2C and WC could be found, whereas at top only WC may be found.

Chapter 5

Conclusion

The study in carbide formation of a-C:W films in an non-thermal equilibrium state have been investigated using XRD, SEM/STEM and nano-diffraction. Within the a-C:W films all three carbides depending on two parameters (concentration and temperature) are observed, although only the stable thermodynamic phase WC is expected. From all carbides, WC_{1-x} is the only and dominant phase at temperatures of 2200K up to 2800K within the lower concentrated films (<10 at.%) (figure 5.1). In the middle concentrated films (10-18 at.%) in the range of 1450K up to 2200K, W_2C is the most common carbide. Only in the higher concentrated films and annealed samples WC begins to become the dominant phase. The presence of WC in the annealed samples is not surprising due to the W-C phase diagram. However, the presence of WC_{1-x} and W_2C are astonishing, as they are not stable below 2789K respectively 1323K. Surprise

In the majority of the samples a mixture of two carbides can be observed, whereas in only a small number of samples all three carbides can be detected. A few samples contain a mixture of WC and WC_{1-x}. The majority of the samples consist out of a mixture between W_2C and WC, respectively WC and WC_{1-x}. W_2C is never observed in large quantities within any sample. The average crystal size of W_2C never exceeds 20 nm, indicating that W_2C and perhaps WC_{1-x} might be transit phase to form WC, as discussed by Jens Luthin [15]. XRD confirms that the 2500K sample of respectively 10% and 12% a-C:W films show diffraction pattern of all three carbides within a single diffractogram. At higher temperatures the WC_{1-x} phase might increase, whereas the W_2C phase will decrease. Nevertheless, WC_{1-x} can be observed alone without the presence of any other carbide in the 6 at.% 2500K sample. Its crystal sizes increase at higher temperature with a maximum average size of ~100 nm.

Grain sizes do not only increase as function of temperature but also as function of concentration. The special designed multi-layer annealed to 2200K clearly proves that the crystal sizes depend on the tungsten concentration in a sample. In addition the multi-layer shows that at a certain concentration (around ~19 at.%) a rapid increase in size occurs. In addition the rate of crystal size growth depends on the type of carbide as seen within the 6 at.% and 9at.% sample.

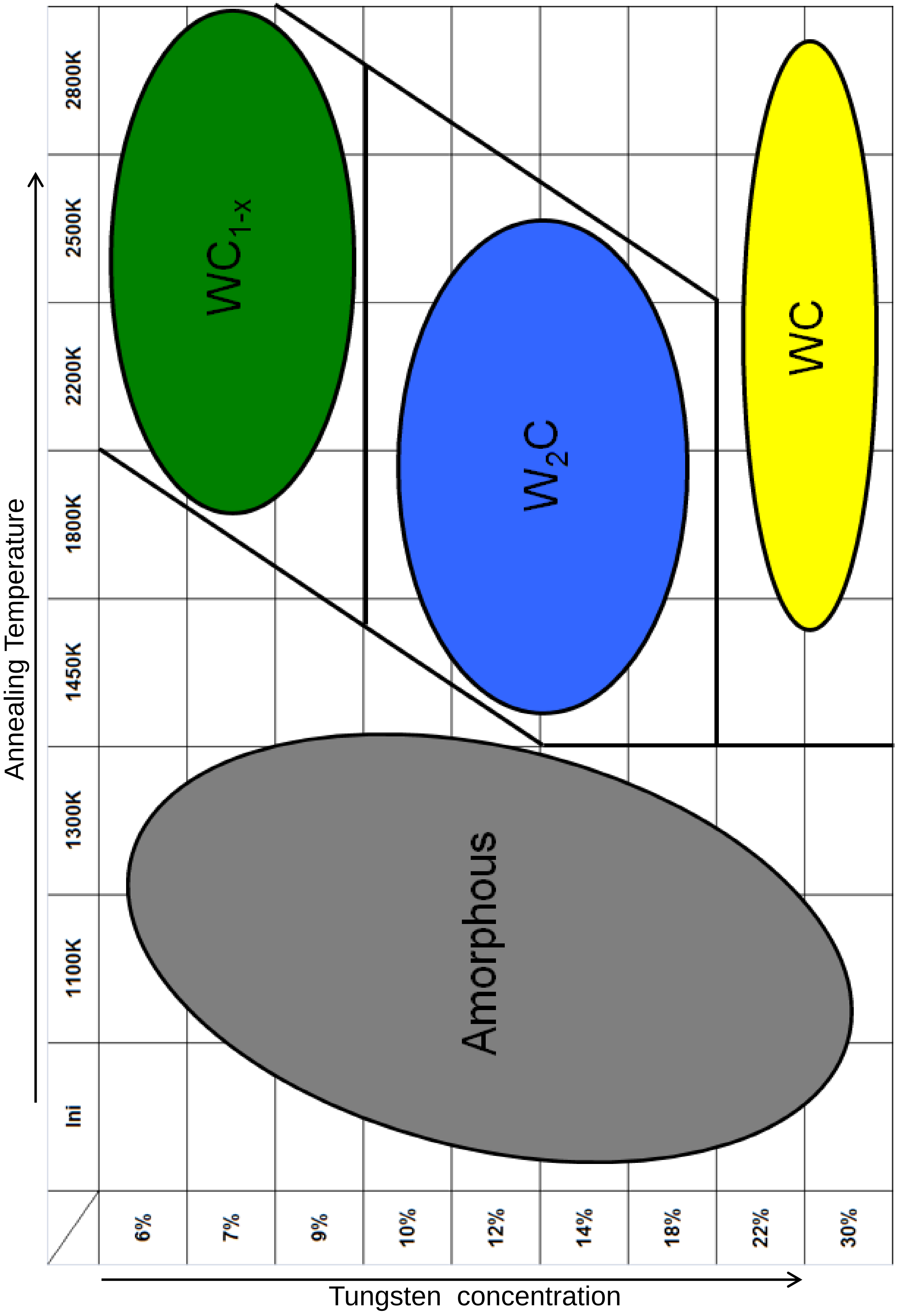

Figure 5.1: summary Tableau

To understand the formation of the cubic WC_{1-x} and hexagonal W_2C and this unusual behavior a hypothesis has been made: during deposition, both carbon and tungsten atoms are distributed randomly throughout the sputter chamber and on the substrate. Depending on the crystal structure, each atom has around 8-12 neighbors. In samples containing low tungsten concentrations (< 9 at.%), it is unlikely to find two tungsten atoms alongside each other. This means, that almost every tungsten atoms is surrounded by a carbon atom. Therefore, the formation of WC_{1-x} and W_2C in the lower concentrated specimen seems illogical. At higher concentrations (~ 22 at.%) each crystal cell should consist out of a minimum of two tungsten atoms. Thus the formation of W_2C and WC_{1-x} would be expected.

Throughout the deposition run, the substrate temperatures do not reach high enough temperatures for crystalline structures to form. Only during heat treatment do the temperatures suffice for crystalline structures to form. Here, the carbon atoms diffuse through the deposited layer, as the process of transporting carbon atoms requires less thermal energy than that of tungsten. Meanwhile the tungsten atoms begin to bond with their neighboring carbon atoms. Depending on the amount of tungsten and carbon atoms in the area, WC_{1-x} or W_2C is formed. As higher temperatures are reached, tungsten atoms also begin to diffuse and bond with the carbon atoms; hence more WC_{1-x} and W_2C is created. In lower concentrated films, the amount of W_2C is too little to be detected by XRD since the crystals remain very small. At concentrations of 14 at.% and higher no more WC_{1-x} is formed and only W_2C is formed. As temperatures and concentration increase, the amount of WC increases as well. Due to the maximal crystal size of W_2C it confirms that W_2C can change its crystal structure easily and rapidly into hexagonal WC.

Why the formation of W_2C is preferred above WC is unknown, however for the stable WC to be formed in a non-thermodynamic equilibrium it is believed that is has to surpass the meta-stable W_2C. Whether WC_{1-x} will change into WC remains unknown, hence further investigation will be needed to understand the carbide formation in a non-thermodynamic equilibrium state.

Chapter 6

Outlook

Even though this investigation has contributed in the study of carbide formation in a-C:W films in a non-equilibrium system, further investigations regarding both temperature and concentration parameter are needed. These investigations should then reveal if the system will change into its thermal equilibrium state, i.e. WC becomes the dominant phase at higher temperatures. Furthermore, it may explain why the carbide formation of high concentrated films takes place earlier at lower temperatures.

A continuing cooperation with Warsaw Technical University, for nano-diffraction on samples, might reveal information about the formation of tungsten carbide crystallites, especially in the multi-layer sample. Secondly, nano-diffraction will complete the SEM tableau giving more information about carbide formation on atomic scale. Besides nano-diffraction, cross-sections on other samples will contribute in completing the SEM tableau. Finally, more special designed multi-layer may contribute in further research in crystal size gradient.

Further research and experience will allow production of special designed layers in the future. Materials containing, meta-stable W_2C, WC_{1-x}, stable WC or a mixture of both will be used for Industrial applications. Besides carbide phases, the crystal sizes for each carbide can be controlled as well. No industrial applications are known for the moment, but might change in course of time.

References

[1] International Energy Agency (IEA), *World Energy Outlook 2008*

[2] ITER homepage, *www.iter.org*

[3] C. Adelhelm, *Structure and Erosion Behavior of Metal-doped Carbon Films,* IPP Report Nr: 17/11

[4] J. Roth et al., *Status of knowledge of chemical erosion of carbon and critical issues for extrapolation to ITER,* J. Nucl. Mater. 390–391 (2009)

[5] A. Kirschner, *Erosion and deposition mechanisms in fusion plasmas,* FST v57 n2T paper: 277-292

[6] M. Balden, *Characterization of nano-structured W-, Ti-, V-, and Zr-doped carbon films,* TSF 519 (2011) 4032-4036

[7] I. Quintana Alonso Thesis, *Production and characterization of metal-doped carbon films*, Universidad de Navarra, San Sebastian (2004)

[8] R. Behrisch, *Sputtering by Particle Bombardment II*, ed. by R. Behrisch, Topics Appl. Phys., Vol. 52 (Springer, Berlin, Heidelberg, 1983)

[9] J.W. Mayer and J.F. Ziegler, *Ionic beam Surface layers Analysis*, ed. by J. W. Mayer and J. F. Ziegler (Elsevier, Lausanne, 1974)

[10] *http://home.rzg.mpg.de/~mam/*

[11] L.A. Giannuzzi & F.A. Stevie, *Introduction to Focused Ion Beams,* (Springer 2005)

[12] B.D. Cullity, *Elements of X-Ray Diffraction*, (Addison-Wesley America 1967)

[13] M. Birkholz, *Thin Film Analysis by X-ray Scattering*, (WILEY-VHC, Weinheim 2006)

[14] ICDD Powder Diffraction File, *www.icdd.com*

[15] J. Luthin, Untersuchung zur chemischen Wechselwirkung bei der Bildung von Kohlenstoff-Mischsystemen, Max-Planck.Institut für Plasmaphysik 2001, IPP Report Nr: 9/129

[16] E. Raekelboom, *Structural investigation by the Rietveld method of sputtered tungsten carbide thin films,* TSF 517 (2009) 1555-8

[17] H. Okamoto, *W-C phase diagram,* JPEDAV (2008) 29:543–544

[18] M. Rasinski, T. Plocinski, M. Balden, C. Adelhelm, M. Lewandowska and K. J. Kurzydlowski, *High resolution analysis of tungsten doped amorphous carbon thin*

films. Proceedings to "2nd International Workshop for Young Materials Scientists", 2010-08-31 to 2010-09-03, Berlin, to be published by Springer Verlag

[19] M. Balden, P.A. Sauter, S. Jong, C. Adelhelm, S. Lindig, M. Rasinski, T. Plocinski, *Carbide formation in tungsten-containing amorphous carbon films by annealing*, Thin Solid Films 519 (2011) 4049

[20] *www.umms.sav.sk/data/files/167.jpg*

[21] *www.ipp.mpg.de/ippcms/de/for/bereiche/material/projekte/msc/5beschichtungen.html*

[22] *http://meyweb.physik.uni-giessen.de/1_Forschung/RBS/kinematik.gif*

Acknowledgement

In this acknowledgement I would like to thank everybody whom has supported, supervised and motivated me during my Bachelor thesis. I especially would like to thank Max-Planck-Institut für Plasmaphysik for giving me the opportunity to perform my thesis at the department Plasma Edge and Wall under director Prof. Stroth.

From all personnel, I would like to thank my supervisor Dr. M. Balden for supporting and motivating me during my Bachelor thesis. I will never forget your confidence in me, technical knowledge, your inspiration, experimental support and helpful discussions that you showed for me during my thesis.

I also would like to thank F. Koch, S. Lindig, A. Manhard, G. Matern, P. Sauter, T. Höschen, M. Fusseder, S. Kimmig, J. Brinkmann, C. Linsmeier and M. Rasinski for their assistance, patience and instructing me using the institute's instruments during this thesis. Also, the many conversations helped me viewing my work from a different perspective allowing me to continue and approach certain problems differently. Finally I would like to thank all personnel of the Plasma Edge and Wall department for their warm welcome and friendly working environment.

Then I would like to thank my supervisor Dr.-Ing U. Koch from the University of Applied Science for scientifically supervising me during this work.

As last I would like to thank my family and friends for supporting and motivating me during my work.